Box Model Intercomparison of Cloud Chemistry

Mary Barth, Barbara Ervens, Hartmut Herrmann, Andreas Tilgner, V. Faye Mcneill, William Gang Tsui, Laurent Deguillaume, Nadine Chaumerliac, Annmarie Carlton, Sara Lance

▶ **To cite this version:**

Mary Barth, Barbara Ervens, Hartmut Herrmann, Andreas Tilgner, V. Faye Mcneill, et al.. Box Model Intercomparison of Cloud Chemistry. Journal of Geophysical Research: Atmospheres, 2021, 126 (21), 10.1029/2021JD035486 . hal-03449947

HAL Id: hal-03449947
https://uca.hal.science/hal-03449947

Submitted on 7 Aug 2022

HAL is a multi-disciplinary open access archive for the deposit and dissemination of scientific research documents, whether they are published or not. The documents may come from teaching and research institutions in France or abroad, or from public or private research centers.

L'archive ouverte pluridisciplinaire **HAL**, est destinée au dépôt et à la diffusion de documents scientifiques de niveau recherche, publiés ou non, émanant des établissements d'enseignement et de recherche français ou étrangers, des laboratoires publics ou privés.

Copyright

Check for updates

JGR Atmospheres

RESEARCH ARTICLE
10.1029/2021JD035486

Key Points:

- Five box models participated in a cloud chemistry intercomparison representing a case at Whiteface Mountain Observatory
- Model results were often quite different indicating a need for recommended equilibria and aqueous-phase reaction rate constants
- Comparisons of simple to detailed chemistry schemes show need for development of effective simplified organic aqueous chemistry schemes

Supporting Information:

Supporting Information may be found in the online version of this article.

Correspondence to:

M. C. Barth,
barthm@ucar.edu

Citation:

Barth, M. C., Ervens, B., Herrmann, H., Tilgner, A., McNeill, V. F., Tsui, W. G., et al. (2021). Box model intercomparison of cloud chemistry. *Journal of Geophysical Research: Atmospheres*, *126*, e2021JD035486. https://doi.org/10.1029/2021JD035486

Received 29 JUN 2021
Accepted 4 OCT 2021

Author Contributions:

Conceptualization: Mary C. Barth, Barbara Ervens, Annmarie Carlton, Sara M. Lance
Formal analysis: Mary C. Barth
Investigation: Barbara Ervens, Hartmut Herrmann, Andreas Tilgner, V. Faye McNeill, William Gang Tsui, Laurent Deguillaume, Nadine Chaumerliac
Methodology: Mary C. Barth, Barbara Ervens, Hartmut Herrmann, Andreas Tilgner, V. Faye McNeill, Laurent Deguillaume, Annmarie Carlton
Project Administration: Mary C. Barth
Writing – original draft: Mary C. Barth
Writing – review & editing: Mary C. Barth, Barbara Ervens, Hartmut

© 2021. American Geophysical Union. All Rights Reserved.

Box Model Intercomparison of Cloud Chemistry

Mary C. Barth[1], Barbara Ervens[2], Hartmut Herrmann[3], Andreas Tilgner[3], V. Faye McNeill[4], William Gang Tsui[4], Laurent Deguillaume[5], Nadine Chaumerliac[5], Annmarie Carlton[6], and Sara M. Lance[7]

[1]National Center for Atmospheric Research, Boulder, CO, USA, [2]Université Clermont Auvergne, CNRS, Sigma-Clermont, Institut de Chimie de Clermont-Ferrand, Clermont-Ferrand, France, [3]Atmospheric Chemistry Department (ACD), Leibniz Institute for Tropospheric Research (TROPOS), Leipzig, Germany, [4]Department of Chemical Engineering, Columbia University, New York, NY, USA, [5]Laboratoire de Météorologie Physique, Université Clermont Auvergne, CNRS, Clermont Ferrand, France, [6]Department of Chemistry, University of California, Irvine, CA, USA, [7]Atmospheric Sciences Research Center, University at Albany, State University of New York, Albany, NY, USA

Abstract Chemical processes in clouds and fogs can substantially alter atmospheric oxidant budgets and lead to aerosol mass formation. However, many regional and global models do not include detailed aqueous-phase chemical mechanisms due to the (a) lack of complete understanding of the chemical processes and (b) computational burden of adding constituents. Current gas-aqueous chemistry 0-dimensional models were evaluated in a cloud-chemistry box model intercomparison based on a mid-September 2016 cloud chemistry event at Whiteface Mountain, New York. Multiphase mechanisms in the five participating models ranged from those appropriate for 3-d models to highly complex with thousands of reactions. This study focused on oxidant levels in both phases and aqueous-phase sulfate and organic acid formation. Comparison of gas-phase-only chemistry gives very similar oxidant predictions at night but shows significant differences during daytime with the hydroxyl radical (OH) variability of about an order of magnitude. The variability in the model results increases substantially with aqueous chemistry due to different Henry's Law constants, aqueous-phase reaction rate constants, and chemical mechanisms. Using a prescribed liquid water content and pH value of 4.5, modeled aqueous OH, aldehyde, and organic acid concentrations differ by over an order of magnitude in daytime. Simulations were also conducted at a pH = 5.1, predicted variable pH, and with added transition metal ion chemistry. While we compare predicted and measured inorganic anions and water-soluble organic carbon, we cannot do so for aqueous-phase oxidant concentrations due to the lack of measurements. We highlight a need for recommended equilibrium and aqueous-phase rate constants.

Plain Language Summary Accurate description of cloud chemistry is needed in models used to predict air quality and climate. A comprehensive international cloud box model intercomparison with physical and chemical observational constraints from mountain top sampling highlights the need for a concerted effort to develop robust aqueous-phase chemical mechanisms. Prediction of some key species differ among the models by orders of magnitude. We investigate the underlying, fundamental chemical explanations for the discrepancy as a diagnosis to understand the chemical parameters most in need of further investigation efforts.

1. Introduction

For several decades, it has been recognized that clouds affect the composition of the atmosphere. They are the primary means by which constituents from the planetary boundary layer (PBL) are lofted to the free troposphere (FT; Chatfield & Crutzen, 1984; Ching et al., 1988; Dickerson et al., 1987). In addition, clouds play an important role as atmospheric aqueous-phase reactors by scavenging soluble gas-phase precursors of ozone and aerosols and supporting oxidation reactions that yield lower volatility products, which contribute to increased aerosol mass when the cloud droplets evaporate. In the 1980s, laboratory and chamber studies, mountain top and aircraft observations, and cloud chemistry modeling studies highlighted the role of aqueous-phase chemistry in cloud and rain drops on the production of sulfate (SO_4^{2-}) from sulfur dioxide (SO_2). While our knowledge of SO_2 to SO_4^{2-} conversion is very good and suitable parameterizations exist (Ervens, 2015), as shown by model-observation and model-model comparisons (e.g., Lamarque et al., 2013), its chemistry continues to be discussed in terms of transition metal ion catalyzed S(VI) production and

Herrmann, Andreas Tilgner, V. Faye McNeill, William Gang Tsui, Laurent Deguillaume, Annmarie Carlton, Sara M. Lance

investigated for intensely polluted regions where nitrogen oxides (NO_x), ammonia (NH_3), and SO_2 have very high abundances (e.g., Xue et al., 2016).

Aqueous-phase oxidation of aldehydes in clouds has been recognized to produce organic acids, initially with formaldehyde conversion to formic acid (Chameides, 1984), but also for difunctional aldehydes oxidation to organic acids (Altieri et al., 2006; Blando & Turpin, 2000; Ervens et al., 2008; Y. Li et al., 2017; Lin et al., 2014; McNeill, 2015; Tilgner & Herrmann, 2010). Laboratory studies showed aldehydes, for example, glyoxal (CHOCHO), undergo hydroxyl radical (OH) oxidation in the aqueous phase to ultimately form dicarboxylic acids, which contribute to secondary organic aerosol (SOA) mass (Blando & Turpin, 2000; Ervens et al., 2011; Lim et al., 2010). These studies prompted exploratory global and regional-scale modeling investigations to determine the regional impact of organic aqueous-phase chemistry (e.g., Chen et al., 2007; Fahey et al., 2017; Gong et al., 2011; Leriche et al., 2013; Lin et al., 2014; Rosanka et al., 2020). Mountain tops are excellent locations to observe the outcomes of cloud chemistry because of the ability to sample inflow and in-cloud air parcels throughout the cloud lifetime and collect ample condensed water for analysis. Measurements at Mount Schmücke in Germany during the field investigations of budgets and conversions of particle phase organics in tropospheric cloud processes experiment (FEBUKO; Herrmann, Wolke, et al., 2005) and Hill Cap Cloud Thuringia 2010 (HCCT-2010) field experiments provided evidence of aqueous phase enrichment of carbonyl compounds (van Pinxteren et al., 2005) and increased sulfate and organic aerosol mass concentrations from cloud processing (Schneider et al., 2017; van Pinxteren et al., 2016). Long-term measurements at Puy de Dôme in France (Baray et al., 2020) have also given insight on the oxidative capacity of the cloud water (Bianco et al., 2015) as well as the organic molecular composition (Bianco et al., 2018) and its environmental variability (Deguillaume et al., 2014; Renard et al., 2020). Studies at Whiteface Mountain in New York, USA have focused mostly on inorganic chemistry producing acidic ions (Schwab, Casson, et al., 2016), adding organic carbon composition measurements to the routine measurement suite in 2009 (Lance et al., 2020). Investigations at Mt. Tai in China characterize the inorganic cloud water composition to have a high anthropogenic influence yet still influenced by soil-based ions during spring and winter (Guo et al., 2012). Using box modeling along trajectories to Mt. Tai, Zhu et al. (2020) found that formation of secondary organic aerosol compounds (i.e., low volatility carboxylic acids) occurred via aqueous-phase oxidation in clouds. Examining outcomes of aqueous-phase chemistry in clouds by aircraft allows for different types of clouds to be sampled. Yet aircraft sampling is challenging because of the small sample volumes collected due to the short sampling times spent in cloud. Examples of aircraft measurements providing information on aqueous chemistry include those demonstrating SO_2 oxidation to SO_4^{2-} (e.g., Hegg & Hobbs, 1986), carbonyls in cloud water (S.-M. Li et al., 2008), in-cloud formation of oxalate (e.g., Sorooshian et al., 2006, 2013), and formation of organosulfates and nitrogen containing compounds (Boone et al., 2015).

These cloud chemistry studies have reached similar conclusions that clouds can produce SOA mass via aqueous-phase oxidation (aqSOA). This result has been shown by different models, yet these models have never been compared to assess whether they predict similar pathways for organic acid formation. In this paper, we conduct an intercomparison of five multiphase (i.e., gas and aqueous) chemistry box models to evaluate the current state of knowledge of cloud chemistry emphasizing the production of organic acids. To avoid additional variability among models, aerosol chemistry and physics are not part of the intercomparison. Each model is run for the same configuration so that predicted oxidants and organic acids can be evaluated.

The box model intercomparison has been conducted as an outcome of the Whiteface Mountain (WFM) Cloud Chemistry Workshop (Carlton et al., 2017; Lance et al., 2017) that planned a coordinated cloud chemistry initiative combining analyses of WFM cloud water samples by multi-institute laboratories, modeling, and planning for a field campaign. This study demonstrates such capabilities with the box modeling and cloud water sample analyses and can be used to inform field campaign planning at WFM. The cloud event of September 17–19, 2016, which occurred immediately after the workshop, is used to configure the model set up. The cloud event consisted of warm-frontal clouds as well as clouds and storms in the warm sector of an extratropical cyclone that was moving from the Midwest into New England and southeast Canada. The clouds were stratiform in nature. Back trajectories from Whiteface Mountain using HYSPLIT (Hybrid Single-Particle Lagrangian Integrated Trajectory) model indicated that the air mass was from the Ohio River

Table 1
General Characteristics of Each Model

Model[a]	Phase transfer	pH calculation	Aqueous-phase organic	Aqueous-phase transition metal ions (TMIs)
CAPRAM	Kinetic Mass Transfer	H^+ predicted	C1–C4 oxidation by OH, NO_3, and partly by O_3, H_2O_2, Cl_2^-, Br_2^-, CO_3^-, SO_4^-, SO_5^-, FeO^{2+}	Fe, Cu, Mn, Fe-oxalate and other MCA/DCA complexes
MCMv3.2 13,927 reactions	275 species			
CAPRAM 4.0α 7129 reactions				
CLEPS				
MCMv3.3.1 (reduced version) 2043 reactions	Kinetic Mass Transfer	H^+ predicted	C1–C4 oxidation by OH, NO_3, O_3, H_2O_2, Cl_2^-, CO_3^-, SO_4^-, FeO^{2+}	Fe, Cu, Mn, oxalate and formic complexes
CLEPS 1.0 1315 reactions	591 species			
GAMMA				
Gas: 165 reactions	Kinetic Mass Transfer	H^+ predicted	C1–C3 oxidation by OH, NO_3, O_3, H_2O_2, SO_4^-, HSO_4^-, IEPOX, organosulfate chemistry	Fe, Cu, Mn, Fe—oxalate complexes
Aq: 185 reactions	30 species			
Barth				
Modified MOZART4 168 reactions	Combination of H_{eff} equilibrium and kinetic mass transfer	Electroneutrality equation	C1–C3 oxidation by OH	None
Aq: 33 reactions	45 species	11 anions		
Ervens				
Gas: Same as Barth	Kinetic Mass Transfer	Electroneutrality equation	C1–C3 oxidation by OH	Fe, Cu
Aq: 58 reactions	22 species	16 anions		

[a]Main references are for CAPRAM Wolke et al. (2005) and Tilgner and Herrmann (2010), for CLEPS Mouchel-Vallon et al. (2017) and Rose et al. (2018), for GAMMA McNeill (2015), for the Barth model Barth et al. (2003) and Y. Li et al. (2017), and for the Ervens model Ervens et al. (2008) and Ervens et al. (2014).

Valley. The cloud water collected from this event was divided into 14 samples and delivered to various laboratories for analysis. When possible, the box model results are compared with the cloud water composition measurements.

The chemistry in the five box models ranged from highly detailed (with thousands of reactions) to moderately detailed (with dozens to hundreds of reactions). After describing the box models and configuration of the simulations (Sections 2 and 3, respectively), we describe in Section 4 results from model simulations for constrained environmental conditions, such as prescribed liquid water content (LWC) and pH of the cloud drops, and less constrained conditions, for example, calculating pH or including transition metal ion chemistry. Reasons for differences among the five models are provided. We conclude the work with recommendations for future field and modeling studies.

2. Description of the Box Models

The five box models evaluated are CAPRAM (Chemical Aqueous Phase Radical Mechanism), CLEPS (Cloud Explicit Physico-chemical Scheme), GAMMA (Gas-Aerosol Model for Mechanism Analysis), Barth, and Ervens. Their gas and aqueous phase chemical mechanisms are described below. General characteristics of each model are given in Table 1. The loss of OH (aq) by water-soluble organic compounds (WSOC), in addition to those that are explicitly included, has been shown to be important to include in cloud and fog drops to better represent OH (aq) concentrations (Arakaki et al., 2013; Tilgner & Herrmann, 2018). The control simulations performed here did not include an aqueous-phase conversion of OH to hydroperoxyl radical (HO_2) by all dissolved WSOC, except for the CAPRAM model. Sensitivity simulations by three of the box models (Ervens, CLEPS, and GAMMA) show that inclusion of WSOC + OH in the aqueous phase has a negligible effect on predicted concentrations of OH (aq), other oxidants, and organic acids because of the low cloud water concentrations of WSOC estimated for the case study. Thus, differences of results between models are not influenced by whether WSOC + OH (aq) is included in the model chemistry mechanism or

not. However, it should be noted that inclusion of WSOC + OH in aqueous-phase mechanism is only negligible under diluted cloud conditions due to the presence of other OH sinks, it is not true under deliquesced aerosol conditions (Tilgner & Herrmann, 2018).

2.1. CAPRAM

The model results from CAPRAM are represented by the SPectral Aerosol Cloud Chemistry Interaction Model (SPACCIM, Wolke et al., 2005; Sehili et al., 2005; Tilgner & Herrmann, 2010 and references therein), which is an adiabatic air parcel model that combines gas, aerosol, and cloud chemistry and physics (Simmel & Wurzler, 2006; Simmel et al., 2005). To best match the instructions of the model intercomparison study, the moving bin version of SPACCIM was applied considering a monodisperse aerosol/cloud spectrum. Microphysical processes, such as impaction of aerosol particles and collision/coalescence of droplets and thus precipitation, were not included here. The interaction between the chemistry and microphysical models occurs via a coupling scheme, which enables both models to run almost separately using their own time step control. For this study, coupling is used but is not important because of the prescribed, constant microphysical conditions.

The chemistry part of the SPACCIM model (CAPRAM in Table 1) treats the gas-phase chemistry, phase transfers, and the aqueous-phase chemistry in both deliquesced particles and liquid cloud droplets, using a high-order implicit time integration scheme (Wolke & Knoth, 2002), which is a modified version of the Livermore ODE solver (LSODE, Hindmarsh, 1983). The chemistry mechanism uses the Master Chemical Mechanism (MCMv3.2; http://mcm.leeds.ac.uk/MCMv3.2/) for gas-phase chemistry and CAPRAM4.0 for aqueous-phase chemistry (Bräuer, 2015; Bräuer et al., 2019), comprising 21,331 multiphase processes and a reaction module that treats non-radical reactions of organic compounds. Gas-aqueous phase transfer processes of 275 inorganic and organic compounds are calculated according to the resistance model of Schwartz (1986). The acidity of the aqueous phase is determined from explicit calculation of the hydrogen ion concentration. In addition to complex inorganic chemistry (Ervens, George, et al., 2003; Herrmann, Tilgner, et al., 2005), CAPRAM contains an explicit chemistry description of C1- C4 organic compounds including branched radical attack (mainly by OH and NO_3), peroxy-radical cross reactions, and the formation of organic nitrates. The non-radical organic chemistry reaction module, coupled to the MCMv3.2/CAPRAM4.0, contains 103 additional reactions of carbonyl compounds and organic acids such as methacrolein, methyl vinyl ketone, acrylic acid, methacrylic acid, pyruvic acid, glyoxylic acid. There are 22 updated OH and NO_3 reactions, SO_4^- radical reactions, and non-radical oxidations by H_2O_2 and O_3 as well as oligomerizations and NH_4^+-catalyzed reactions considered. For the model intercomparison, inorganic and organic chemistry based on the initial chemical trace gases were used, including WSOC + OH → WSOC + HO_2. Further details on the CAPRAM mechanism are given in Ervens, George, et al. (2003), Herrmann, Tilgner, et al. (2005), Weller et al. (2014), Bräuer (2015), and Bräuer et al. (2019).

CAPRAM considers an inorganic core mechanism which includes important TMI reactions of iron, copper, and manganese (e.g., Ervens, George, et al., 2003; Weller et al., 2014). The redox chemistry scheme of iron, copper, and manganese includes a detailed description of (a) TMI reactions with key aqueous-phase oxidants, such as HO_2/O_2^- and H_2O_2, (b) TMI-TMI redox reactions, (c) TMI-catalyzed reactions with various sulfur species and (d) chemical processes with oxygenated organic compounds. The CAPRAM TMI chemistry includes 92 bimolecular reactions and 26 equilibrium reactions. CAPRAM also treats important photolysis reactions of iron(III)hydroxides, iron(III)sulfate, as well as the formation and photolysis of iron-organic-complexes. Overall, 15 photolysis processes of metal complexes including both iron-organic-complexes and inorganic TMI complexes are considered. Due to the focus of the present study on the chemical mechanism aspects, the applied model framework is addressed hereafter as the CAPRAM model.

2.2. CLEPS

The CLEPS model is a highly detailed multiphase chemistry model coupled with a two-moment, liquid-only microphysical module that includes the activation of aerosol particles into cloud droplets and drop condensation, collision/coalescence, and evaporation (Leriche et al., 2007; Rose et al., 2018). In this work, only the multiphase chemistry is simulated using prescribed conditions as outlined in Section 3.

The multiphase chemistry is solved using the Rosenbrock methods provided with the kinetic pre-processor v2.1 (Sandu & Sander, 2006). The gas-phase chemistry used by CLEPS is the MCM3.3.1 mechanism (Jenkin et al., 2015; Saunders et al., 2003), which is built on the MCM web site considering specific precursors (alkanes, alcohols, carbonyls, carboxylic acids, hydroperoxides, and inorganic species) and includes the treatment of isoprene oxidation products. This gas-phase mechanism has been used to simulate low-NO_x chemical environments with CLEPS (Mouchel-Vallon et al., 2017; Rose et al., 2018). The CLEPS model simulations use in-model calculated photolysis rates instead of the prescribed photolysis rates used by the other models. In the CLEPS photolysis rate module, actinic flux is calculated by the Troposphere Ultraviolet and Visible radiation model (TUV v4.5), and quantum yields and cross-sections are from experimental data (Deguillaume et al., 2004; Long et al., 2013). A comparison of CLEPS photolysis rates and those prescribed for these simulations is shown in Supporting Information S2 for O_3 forming O^1D, NO_2, and H_2O_2.

All gases (591 species) are dissolved in the droplets even if they are not further oxidized in the aqueous phase. Conversely, some aqueous species described in CLEPS can be outgassed even if there is no corresponding gas species in MCM. All species have an equivalent in the respective other phase, even if the species in the other phase is not reactive. Phase transfer processes are calculated according to the resistance model of Schwartz (1986) considering the gas-phase diffusion coefficient, the mass accommodation coefficient, and the Henry's Law coefficient. Henry's law coefficients not available in the literature are provided by the GROMHE structure activity relationships (SARs) (Raventos-Duran et al., 2010). When unavailable, their temperature dependencies (enthalpy of dissolution) are set to 50 kJ mol^{-1}.

Aqueous-phase chemistry in CLEPS includes detailed inorganic and organic chemistry. The inorganic mechanism simulates the redox processes involved in the evolution of H_xO_y, sulfur, nitrogen, halogen (Leriche et al., 2000, 2003, 2007) and TMI (Deguillaume et al., 2004; Long et al., 2013) compounds. The CLEPS mechanism is extended to the oxidation of C1-C4 precursors and follows the protocol described in Mouchel-Vallon et al. (2017). For each species and its oxidation products, the CLEPS mechanism describes the oxidation of OH and NO_3 and the explicit evolution of the produced peroxyl radicals. When data are available, the reactivity of organic compounds with other oxidants (e.g., SO_4^- and Cl_2^-) is also addressed. Hydration and dissociation equilibria are, respectively, considered for carbonyl and carboxylic functions. Recent developments in empirical estimates of kinetic and thermodynamic parameters (e.g., rate constants, Henry's law constants) for aqueous phase chemistry (Doussin & Monod, 2013; Minakata et al., 2009; Monod & Doussin, 2008; Raventos-Duran et al., 2010) are included in the CLEPS mechanism using SARs, which provide estimations of reaction rate and equilibrium constants, as well as the branching ratios between the different oxidation pathways with OH radicals (Doussin & Monod, 2013; Minakata et al., 2009).

The TMI chemistry, included in a sensitivity simulation, represents iron (Fe(II), Fe(III), and Fe(IV)), copper (Cu(I) and Cu(II)), and manganese (Mn(II) and Mn(III)) reactions with H_xO_y, sulfur, NO_y and VOCs, as well as photolysis of the TMIs (Deguillaume et al., 2004, 2005; Long et al., 2013). In the TMI module, iron reactions include photolysis of Fe(III), Fe(II) oxidation by H_2O_2 via Fenton reaction and by OH as well as O_3. Fe(III) can form various complexes with oxalate, which can oxidize to form the $C_2O_4^-$ radical. Copper reactions involve the oxidation and reduction of Cu(I) and Cu(II), respectively, with HO_2 and O_2^- radicals. Reactions between Fe(III) and Cu(I) that yield Fe(II) and Cu(II) are included as they modify iron reactivity. Manganese reactions also involve HO_2, O_2^-, H_2O_2, and O_3. Conversion of sulfite into sulfate occurs via oxidation by dissolved oxygen, catalyzed by transition metals, in particular by iron and manganese.

2.3. GAMMA

The GAMMA model is a photochemical box model that predicts aerosol and cloud water composition under different atmospheric and laboratory conditions (McNeill, 2015). GAMMA uses a user-specified surface area-averaged ammonium sulfate aerosol radius to determine multiphase mass transfer parameters and a scaling factor defined from liquid water content for cloud droplet size (Tsui et al., 2019).

GAMMA solves the differential equations for multiphase chemistry using the ode15s MATLAB solver, which is an implicit, variable-step, variable-order solver for stiff sets of ODEs. The gas-phase mechanism in GAMMA 5.0 (Tsui et al., 2019) represents the oxidation of the C1-C3 volatile organic compounds (VOCs) as well as VOCs such as isoprene, acetylene, toluene, and xylenes that form highly soluble products such

as glyoxal and epoxides. Gas-aqueous phase transfer of 30 inorganic and organic compounds are computed following the resistance model of Schwartz (1986). In addition to the TMI inorganic chemistry described below, GAMMA includes the formation of sulfate and bisulfate radicals through oxidation of bisulfate and sulfuric acid by OH. These inorganic radicals can then oxidize organic species to form organosulfates. The aqueous phase mechanism includes OH, HO_2, NO_3, O_3, H_2O_2, SO_4^-, and HSO_4^- radical oxidation of C1-C3 carbonyls, organosulfate formation from photochemical radical and epoxide mechanisms, and IEPOX SOA formation (McNeill, 2015; McNeill et al., 2012).

The TMI chemistry, included in a sensitivity simulation, represents iron (Fe(II) and Fe(III)), copper (Cu(I) and Cu(II)), and manganese (Mn(II), Mn(III), and Mn(IV)) reactions with OH, HO_2, O_2^-, and H_2O_2, TMI-TMI reactions, and TMI-catalyzed reactions. Iron reactions include oxidation by H_2O_2 as in the Fenton reaction as well as O_2^- and HO_x radicals and the formation of complexes with sulfate and oxalate. No sulfate or oxalate complexes are included with other transition metal ions, though the reduction of SO_4^- by Cu^+ is included to form sulfate. Copper and manganese reactions primarily include oxidation by HO_x and H_2O_2 and reactions with other TMIs.

2.4. Barth

The Barth box model is designed to mimic how a three-dimensional chemistry transport model would represent multiphase chemistry. That is, the 3-d model predicts the thermodynamic variables and liquid water content that are provided to the chemistry module. In the Barth box model, thermodynamic variables and liquid water content are prescribed.

The multiphase chemistry is solved using the Euler backward iterative (EBI) method, which is a stable, implicit method that was shown to perform similarly to high-order, ODE solvers (Barth et al., 2003). The Barth box model employs the gas-phase chemistry mechanism used in the NCAR large-eddy simulation (LES) coupled with chemistry (LES-chem) (Kim et al., 2012). It includes 64 reactants and 168 reactions that are based on MOZART2.2 (Horowitz et al., 2003) and MOZART4 (Emmons et al., 2010). Gas-aqueous partitioning is either described according to Henry's Law coefficients for low solubility or slowly reacting compounds or, it is calculated according to the resistance model of Schwartz (1986) for high solubility (HNO_3) or fast reacting (OH, HO_2, and NO_3) compounds. More details on this methodology can be found in Barth et al. (2001, 2003). The aqueous-phase chemical mechanism is a modification of that described by Y. Li et al. (2017) who examined the effect of aqueous-phase chemistry on biogenic volatile organic compounds using the NCAR LES-chem model. The aqueous chemistry species include simple sulfur, ozone (O_3), and organic aldehydes, peroxides, and acids. Oxidation of C1-C3 carbonyls and organic acids is by OH only. Modifications from Y. Li et al. (2017) include removing H_2O_2 reactions with glyoxal, glyoxylic acid, formic acid, oxalic acid, and pyruvic acid, removing OH reactions with methanol, acetone, isoprene, methacrolein, and methyl vinyl ketone, and removing O_3 reactions with methacrolein and methyl vinyl ketone. Oxidation of acetic acid by OH was modified to produce glyoxal instead of glycolaldehyde, and methyl hydrogen peroxide (CH_3OOH) oxidation by OH was modified to produce formic acid instead of formaldehyde following Ervens et al. (2008). Transition metal ion chemistry is not included in the aqueous-phase mechanism, nor is WSOC + OH.

2.5. Ervens

The Ervens model (Ervens et al., 2008, 2014) is based on an adiabatic air parcel model (Feingold et al., 1998). However, for this model intercomparison, no microphysical processes are calculated, but instead the model uses prescribed LWC. The LWC is distributed to a number of droplets that is determined by the LWC to drop volume ratio where the radius $r = 10$ μm.

The Ervens box model uses a VODE solver with a model time step of 2 s. For this model intercomparison, the gas-phase mechanism used by the Barth box model (Kim et al., 2012) is adopted. Gas-aqueous phase transfer processes of 22 inorganic and organic compounds are described according to the resistance model of Schwartz (1986). The aqueous phase mechanism is based on Ervens et al. (2008, 2014). It includes the major sulfur (IV) oxidation pathways and HO_x chemistry, largely based on the first versions of CAPRAM (Ervens, George, et al., 2003). In addition, aqueous-phase glyoxal chemistry based on Lim et al. (2010) was

implemented. The OH radical is assumed to be the only oxidant of organic compounds (C1–C3), leading to the oxidation of aqueous glyoxal and other carbonyls and the formation of di- and keto acids. Aqueous-phase transition metal ion chemistry is included in a sensitivity simulation. The Ervens box model results presented here are based on simulations without the WSOC + OH → WSOC + HO_2 reaction.

The TMI chemistry, included in a sensitivity simulation, represents iron (Fe(II) and Fe(III)) and copper (Cu(I) and Cu(II)) reactions with OH, HO_2, and H_2O_2, and TMI-TMI reactions. Besides Fe(II) oxidation by H_2O_2 via Fenton reaction and by OH, HO_2 and O_3, Fe(III) hydroxy complexes undergo photolysis processes. Cu(I) is oxidized and Cu(II) is reduced via reactions with HO_2 and its anion O_2^-. The TMI module also represents Fe(III) reaction with Cu(I) to form Fe(II) and Cu(II). Note, that manganese is not included in the TMI chemistry module.

3. Conditions of the Simulations and Measurements Used

The box for the model intercomparison was placed at the location of the Whiteface Mountain (WFM) Summit Observatory in New York, USA. This location is defined as 44.4°N, 73.9°W at an altitude of 1,500 m. At WFM Summit Observatory, several parameters are measured routinely including wind direction, wind speed, temperature, relative humidity, cloud liquid water, and trace gas mixing ratios of NO, NO_2, NO_y, O_3, CO (carbon monoxide), and SO_2. Details on the measurement techniques for these parameters are given in Schwab, Casson, et al. (2016) and Schwab, Wolfe, et al. (2016). These quantities were used to initialize the box model simulations.

Cloud water was collected with a Mohnen omni-directional passive cloud water sampler (Falconer & Falconer, 1980; Möhnen & Kadlecek, 1989) with 0.4 mm Teflon strings corresponding to <5 μm droplet cutoff diameter at >5 m s^{-1} wind speeds at WFM Summit Observatory from 18:00 17 September 2016 to 05:00 local time (LT) 19 September 2016. These times match with 2200 UTC and 0900 UTC. On 17 September 2016 at 1200 UTC (0800 LT), a low center of pressure was located over Lake Superior. From this low center a cold front reached southward to Kansas and an occluded front reached eastward. The occluded front had attached both a cold front extending from southern Ontario, Canada southward to Tennessee and a warm front extending to North Carolina. This warm front approached New York bringing stratiform cloud ahead of the front. WFM remained in the warm sector of the extratropical system until about 1400 UTC 19 September 2016. The winds continued to be from the southwest with ample cloud cover.

More than 1.8 L of water was collected for the September 17–18, 2016 cloud event at WFM over a 36-h period. The cloud water was divided into 140 mL vials and sent to various laboratories for chemical analysis. We make use of the following measurements to evaluate the box model results. Cloud water pH is measured by the Adirondack Lakes Survey Corporation (ALSC). ALSC also analyzes the cloud water using ion chromatography for inorganic anions: nitrate, sulfate, chloride, calcium, magnesium, potassium, sodium, and ammonium. Total organic carbon (TOC) in the cloud water was measured by ALSC with atomic absorption, colorimetric, carbon analyzer persulfate oxidation. Dissolved organic carbon (DOC) was measured by the Herckes lab using the technique described by Boris et al. (2016). The Herckes lab used ICP-MS (Straub et al., 2012) to obtain cloud water concentrations of metals. Water soluble organic carbon (WSOC) was measured by the Weber laboratory using Seivers TOC technique (Sullivan et al., 2004). The DOC and WSOC measurements are expected to represent the same property, while TOC can include a contribution from insoluble organic matter. Herckes et al. (2013) showed the DOC is typically within 25% of TOC.

Evaluation of the box model results with measurements of the cloud water composition is challenging for several reasons. First, the cloud water sample represents several hours of collection. The measurements from ALSC are for samples every 12 hr, but those from Herckes and Weber are from the entire cloud event (up to 35 hr of collection). Thus, the measurements reflect an accumulated composition that ideally is represented by the time integration of the box models. Second, the box model is run at a single location with set meteorology throughout the model simulation, while the air sampled at WFM is actually moving with the winds and may have a different history of meteorological conditions than what is modeled. Indeed, it is likely much better to follow a trajectory of air as it enters a cloud from an upwind location and moves to the observation location, as that air parcel along a trajectory will experience mixing and other physical and radiative processes, as well as different aerosol composition over time. Thus, the comparison of model results

Table 2
List of Simulations Performed

Simulation	Gas-phase chemistry	Aqueous-phase chemistry	pH	Aqueous-phase TMI chemistry
1	Yes	No	N/A	No
2	Yes	Yes	4.5	No
3	Yes	Yes	5.1	No
4	Yes	Yes	4.5	Yes
5	Yes	Yes	Calculated	No

with observations will be done to learn whether our current understanding of the cloud water chemistry is similar or very different than what is seen in observations and will not be used to determine if a particular model is better than the others or not.

All simulations begin at 17:30 local time (LT) on September 17, 2016 and end at 15:00 LT September 18, 2016. For this configuration, the simulation begins in daylight 1(1/2) hr before sunset (~19:00 LT), which is followed by ~11(1/2) hr of nighttime and then 8(1/2) hr of daylight. Photolysis rates in all the models except CLEPS were prescribed using values for the location and date of the cloud event from the Troposphere Ultraviolet Visible radiation model (TUV v5.3) for clear sky conditions. The meteorological conditions, obtained from the WFM Summit Observatory data, were prescribed, holding values constant during the simulation. These conditions are temperature = 286 K and pressure = 847 hPa resulting in a dry air density of 1.032 kg m^{-3}, and water vapor = 10.068 g kg^{-1}. Using constant values for the meteorology is justified in that the WFM observations showed that temperature, pressure, and water vapor remained fairly constant during the cloud event. The initial chemical concentrations were obtained from the WFM Summit Observatory for NO, NO_2, NO_y, O_3, CO, or taken from a WRF-Chem simulation, and SO_2 was set to 150 pptv. The WRF-Chem domain was configured for the conterminous U.S. at 12-km horizontal grid spacing and 40 vertical levels from the surface to 50 hPa. The simulation was initialized at 0000 UTC 16 September 2016 and integrated until 0000 UTC 19 September 2016 using GFS meteorological conditions and the global chemistry transport model MOZART chemical conditions. More details on the WRF-Chem simulation are given in Supporting Information S1. WRF-Chem results were extracted from the surface output at the grid point nearest WFM at 2100 UTC 17 September (1700 LT) to initialize the box models. The initial chemical box model conditions can be characterized as continental background with O_3 = 39 ppbv, NO_x = 180 pptv, isoprene = 1 ppbv, monoterpenes = 40 pptv, carbon monoxide = 140 ppbv, ethane = 850 pptv, and SO_2 = 150 pptv. The model conditions are given in Tables S1–S6 in Supporting Information S3.

Five simulations are conducted (Table 2). Simulations included gas-phase only or gas-cloud chemistry. None of the simulations included aerosol chemistry. Simulation 1 represents clear sky conditions; no cloud chemistry occurred. Simulation 2 prescribes a cloud from 18:00 LT 17 September to 14:00 LT 18 September with a liquid water content of 0.78 g kg^{-1}, which is the average LWC of the observations during this time period. In Simulation 2, the pH is set to 4.5. Simulation three is the same as Simulation 2 but the pH is prescribed to 5.1, which is the average measured pH by ALSC (note, that the measurements from ALSC were not available before the box model intercomparison began). Simulation 4 is the same as Simulation 2 but aqueous-phase TMI chemistry is included. Simulation 5 is the same as Simulation 2 but the pH is calculated by the individual models.

Sources of differences among the model results can be attributed to the chemical mechanism, reaction rate constants and equilibrium coefficients. Note that the environmental conditions (temperature, pressure, liquid water content) are constrained in all five simulations and should not contribute to differences among model results. The chemical mechanisms, and reaction rate and equilibrium coefficients are not constrained for any of the simulations. The equilibrium coefficients may play a significant role in causing differences among model results. Table 3 lists the effective Henry's law constant (H_{eff}) from each model for Simulation 2 conditions (T = 286 K, pH = 4.5). The five models use different equilibrium coefficients for most trace gases. Many H_{eff} values are similar from model to model, but some trace gases have a variety of H_{eff} values. For example, higher H_{eff} values for CH_2O and methylglyoxal (MGLY) are used in the Ervens model compared to CAPRAM, CLEPS, and Barth models, and lower H_{eff} for glycolic acid is used in the Ervens model. To address whether these differences in equilibrium coefficients explain differences in the model results, we perform simulations with the Barth model using the equilibrium coefficients from each model. These results are in the Supporting Information S2 and discussed in Section 4.

The oxidation of aldehydes and organic acids by OH is an important part of the aqueous-phase organic chemistry. The reaction rate constants for these reactions can also contribute to differences between the five models. Table 4 lists the reaction rate constants used by each model for Simulation 2 conditions (T = 286 K).

Table 3
Effective Henry's Law Constant, H_{eff} ($M\ atm^{-1}$), Used in Each Model for T = 286 K and pH = 4.5

Species	CAPRAM	CLEPS	GAMMA	Barth	Ervens
OH	52.6	90.9	59.1	71.4	52.6
HO_2	13,550	2650	1615	3336	13,550
H_2O_2	249,000	215,500	248,000	243,900	249,000
O_3	0.01576	0.01534	0.01570	0.01534	0.01576
CH_3OO	683	[a]	[a]	5.00	310
CH_3OOH	683	650	647	631	310
CH_2O	8290	8770	8920	8780	13,810
CH_3CHO	27.5	29.5	30.5	29.6	11.4
Glycolaldehyde	79,450	71,120	80,000	76,770	41,400
Glyoxal	1.20×10^6	1.20×10^6	1.20×10^6	1.20×10^6	1.20×10^6
Methylglyoxal	10,730	10,710	10,030	10,130	92,530
HYDRALD	[a]	[a]	[a]	256,000	41,400
Formic Acid	80,720	140,600	142,300	140,300	80,600
Acetic Acid	19,630	15,250	15,230	15,400	19,660
Glycolic Acid	283,500	237,400	285,100	166,100	52,830
Glyoxylic Acid	235,500	34,080	350,400	218,700	196,800
Pyruvic Acid	7.20×10^7	3.54×10^7	6.57×10^7	8.23×10^7	8.27×10^7
Oxalic Acid	3.74×10^{12}	5.59×10^{12}	1.70×10^{13}	2.69×10^{12}	4.85×10^7
SO_2	1080	845	1042	1145	1043
HNO_3	6.41×10^{11}	4.97×10^{11}	3.53×10^{11}	4.97×10^{11}	4.97×10^{11}

[a]Methyl peroxy radical (CH_3OO) and/or hydroxy aldehyde (HYDRALD) do not transfer into the aqueous phase.

There are some notable differences among models that can be seen. Aqueous CH_2O oxidation is not included in the GAMMA model. Glycolaldehyde oxidation rate constant is 2.5–5 times smaller in the GAMMA model than the other four models. The MGLY oxidation rate constant is up to two times greater in the CAPRAM and CLEPS models compared to the other three models. In addition, the CAPRAM and CLEPS models treat both the hydrated and unhydrated form of the aldehydes separately, including their different reactivity. These differences must be kept in mind when evaluating the box model results.

In Simulation 5, each model predicted the pH of the cloud water instead of prescribing the pH as was done in Simulations 2–4. The way pH is predicted can also cause differences among the models. The CAPRAM, CLEPS, and GAMMA models explicitly predict the hydrogen ion in the aqueous phase while the Barth and Ervens models use an electroneutrality equation (Table S7 in Supporting Information S3). The electroneutrality equation includes major inorganic cations and anions as well as anions from the organic acids.

4. Results

4.1. Clear-Sky Only Chemistry (Simulation 1)

To gain an understanding of how well the five models agree for just gas-phase conditions, a clear-sky only simulation was conducted for the 21(1/2) hr simulation time period, allowing us to contrast the different model results for nighttime and daytime conditions.

Oxidant (OH, HO_2, H_2O_2, and O_3) concentrations, in general, agree more among the models and with measurements for O_3 during the nighttime hours than during daytime (Figure 1). During nighttime, OH ranges from 1×10^{-3} to 1.5×10^{-3} pptv, while the midday (hour 36) concentrations range from 0.1 to 0.26 pptv. Results for nighttime HO_2 (0.64–1.5 pptv) vary more than midday HO_2 mixing ratios (20–30 pptv). While all models predict 1.24 ppbv of H_2O_2 at night due to its lack of sources and sinks at night, the H_2O_2 mixing

Table 4
Aqueous-Phase Reaction Rate Constants (M^{-1} s^{-1}) at T = 286 K for Each of the Models

Reaction	CAPRAM	CLEPS	GAMMA	Barth	Ervens
Formaldehyde					
CH_2O ($CH_2(OH)_2$) + OH	8.66×10^8	6.78×10^8	Neglected	8.79×10^8	8.65×10^8
Acetaldehyde					
CH_3CHO + OH	3.10×10^9	3.60×10^9			
$CH_2CH(OH)_2$ + OH	1.30×10^9	1.20×10^9			
Effective rate constant			Neglected	3.29×10^9	3.60×10^9
Glycolaldehyde					
CH_2OHCHO + OH	1.37×10^9	1.40×10^9			
$CH_2OHCH(OH)_2$ + OH	1.12×10^9	1.10×10^9			
Effective rate constant			5.00×10^8	1.20×10^9	1.20×10^9
Glyoxal					
CHOCHO + OH	6.60×10^7				
$CHOCH(OH)_2$ + OH	8.89×10^8				
$CH(OH)_2CH(OH)_2$ + OH	8.68×10^8	8.89×10^8			
Effective rate constant			1.10×10^9	7.83×10^8	8.06×10^8
Methylglyoxal					
$CH_3C(O)CHO$ + OH	7.11×10^8				
$CH_3C(O)C(OH)_2$ + OH	6.32×10^8	7.73×10^8			
$CH_3C(OH)_2CHO$ + OH	8.27×10^8				
$CH_3C(OH)_2CH(OH)_2$+ OH	9.81×10^8	7.73×10^8			
Effective rate constant			7.00×10^8	5.76×10^8	8.76×10^8
Formic Acid					
HCOOH + OH	1.13×10^8	8.69×10^7	1.00×10^8	1.13×10^8	1.13×10^8
$HCOO^-$ + OH	2.78×10^9	2.87×10^9	3.10×10^9	2.78×10^9	2.78×10^9
Acetic Acid					
CH_3COOH + OH	1.41×10^7	1.24×10^7	1.60×10^7	1.24×10^7	1.24×10^7
CH_3COO^- + OH	5.69×10^7	7.76×10^7	8.50×10^7	7.76×10^7	7.74×10^7
Glycolic Acid					
$(OH)CH_2COOH$ + OH	6.00×10^8	6.00×10^8	6.00×10^8	5.40×10^8	5.40×10^8
$(OH)CH_2COO^-$ + OH	1.20×10^9	8.60×10^8	8.60×10^8	1.20×10^9	1.20×10^9
Glyoxylic Acid					
(OHC)COOH + OH	1.30×10^8				
$CH(OH)_2COOH$ + OH	3.13×10^8	2.87×10^8			
Effective acid rate constant			3.62×10^8	3.13×10^8	3.12×10^8
$(CHO)COO^-$ + OH	4.46×10^8				
$CH(OH)_2COO^-$ + OH	1.41×10^9	1.36×10^9			
Effective anion rate constant			2.90×10^9	1.58×10^9	1.57×10^9
Pyruvic Acid					
$CH_3C(O)COOH$ + OH	8.09×10^7				
$CH_3C(OH)_2COOH$ + OH	3.15×10^8	2.48×10^8			
Effective acid rate constant			6.00×10^7	2.48×10^8	1.20×10^8
$CH_3C(O)COO^-$ + OH	5.06×10^8				
$CH_3C(OH)_2COO^-$ + OH	5.54×10^8	4.65×10^8			

Table 4
Continued

Reaction	CAPRAM	CLEPS	GAMMA	Barth	Ervens
Effective anion rate constant			6.00×10^7	4.65×10^8	7.00×10^8
Oxalic Acid					
HOOCCOOH + OH	1.40×10^6	Neglected	1.40×10^6	1.40×10^6	1.40×10^6
$HOOCCOO^-$ + OH	1.28×10^8	1.28×10^8	2.00×10^7	1.28×10^8	1.27×10^8
$^-OOCCOO^-$ + OH	8.73×10^7	8.73×10^7	4.00×10^7	8.73×10^7	8.67×10^7

ratios during daytime vary from 1.5 to 3.8 ppbv. Like H_2O_2, O_3 at nighttime is predicted to be approximately the same at night (39 ppbv). After sunrise, the models predict O_3 production in varying amounts while the observations show O_3 loss. The difference between model results and observations is likely due to lower O_3 mixing ratios transported to WFM or missing chemistry. These model results show that the Barth and Ervens models, using the same gas-phase mechanism, have the same results. Although the CAPRAM and CLEPS models utilize the MCM (albeit different versions with the CLEPS model using a reduced mechanism noted in Table 1), the oxidant results from these two models are somewhat different. The differences between CAPRAM and CLEPS highlight the importance of clearly defining the version and configuration of the chemistry mechanism.

The different models have much more variable results for gas-phase aldehyde concentrations (Figure 2) compared to the oxidants. Nighttime CH_2O and CH_3CHO mixing ratios are fairly similar among most models (CH_2O: 2.7–2.9 ppbv, CH_3CHO: 400 pptv for four models and 500 pptv for GAMMA), but daytime concentrations vary much more, ranging for CH_2O from 1.4 to 2.4 ppbv at noon (t = 36 h), and for CH_3CHO 150–550 pptv at noon. Similarly, glycolaldehyde and glyoxal vary among the different models less at night than during day. At night, glycolaldehyde is ~420 pptv and at midday it ranges from 320 to 420 pptv, while the glyoxal range is 200–225 pptv at night and 70–140 pptv at midday. Methylglyoxal shows considerable variation, with different trends in different models. The CLEPS model has methylglyoxal increasing throughout the simulation until late morning (time ~35 h), while the other four models show increasing methylglyoxal at night and decreasing mixing ratios during day.

Only two organic acids, HCOOH and CH_3COOH, are potentially produced in the clear-sky only simulation. HCOOH, initialized at 0 pptv, is not produced in the Barth or Ervens gas-phase chemistry, while it is produced in the other models, generating ~50 pptv by midday (Figure 3). CH_3COOH generally increases throughout the simulation with nighttime mixing ratios increasing from 200 to 210–270 pptv (Figure 3), and daytime CH_3COOH production being anywhere from 20 pptv to 230 pptv.

The variability among models for the gas-phase only simulation will be reflected in differences found in the gas-aqueous chemistry simulations. Being a major aqueous-phase oxidant, the OH variation among models is important. The factor of 1.5 variation at night and 2.6 variation during day for OH among the five models could affect agreement for the cloud simulations. However, it is known that aqueous-phase OH concentrations are controlled by both the gas-to-drop phase transfer and the aqueous-phase chemistry, which could reduce (or enhance) the impact of the gas-phase only variation (e.g., Ervens et al., 2014; Paulson et al., 2019).

4.2. Reference Simulation in Cloud Water (Simulation 2)

By prescribing the liquid water content and the pH, differences among the five models become constrained to differences in the chemical mechanism, reaction rate and equilibrium coefficients. With the onset of cloud, gas-phase OH concentrations (Figure 4) decrease and are more variable among the models compared to the clear-sky simulation, with an order of magnitude variation among models (compared to a factor of 2.6 or less for the clear-sky simulation). These variations are caused by different chemistry represented in each model as the Barth chemistry simulations employing the different equilibrium coefficients used by the other models (Figure S1 in Supporting Information S2) do not show appreciable OH differences among models. This is consistent with mass transport limitations of OH transfer into cloud drops and fast OH

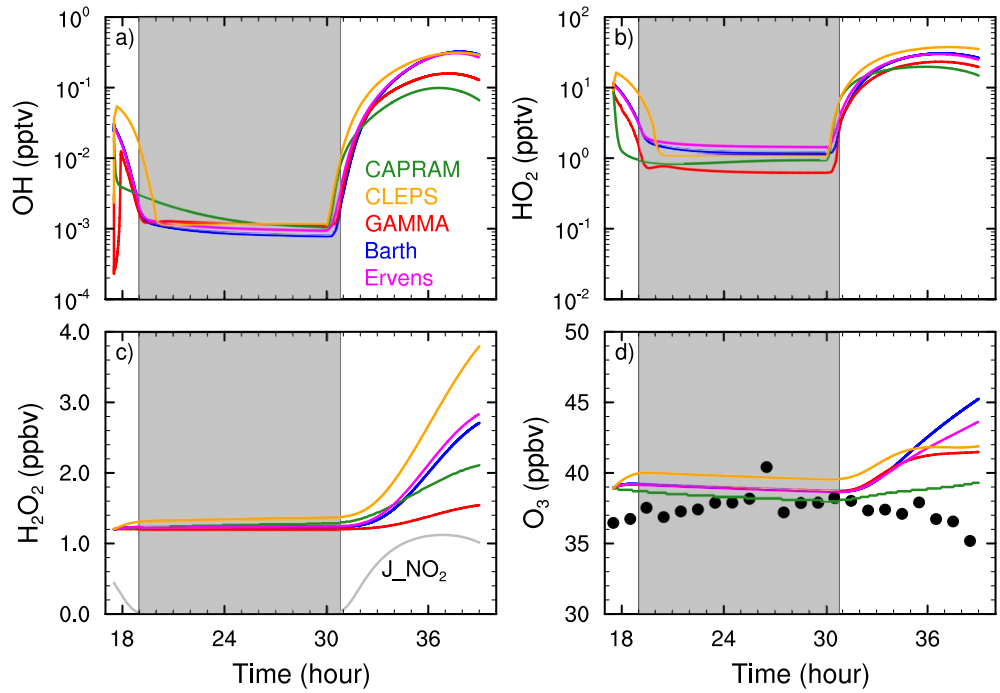

Figure 1. Time series plots for (a) OH, (b), HO_2, (c) H_2O_2, and (d) O_3 gas-phase concentrations from the clear-sky only simulation. Results are colored by different models, where green lines are the CAPRAM, gold lines are CLEPS, red lines are GAMMA, blue lines are Barth, and magenta lines are Ervens models. The gray line in panel (c) is the photolysis rate for NO_2 (0.01 s^{-1}) indicating daylight and nighttime periods. The gray shaded region denotes nighttime. The black dots in the O_3 panel are hourly average observations from the WFM Summit Observatory measured by ASRC.

chemistry. Gas-phase HO_2 mixing ratios (0.5–1.0 pptv at night; 2–10 pptv at midday) are also more variable for the cloud simulation than the clear-sky simulation. Some of the variability may be due to using different equilibrium coefficients (Figure S1 in Supporting Information S2), but the variability is caused more by different chemistry. Gas-phase H_2O_2 mixing ratios at night during the cloud event are quite small (~200 pptv), but increase after sunrise to midday with mixing ratios of 370–540 pptv. After the cloud event, gas-phase H_2O_2 mixing ratios predicted by the different models are substantially different with mixing ratios ranging from 1.6 to 3.8 ppbv. These differences among models are primarily due to different irreversible chemical reactions rather than equilibrium coefficients. Introducing cloud chemistry reduces the production of O_3 (Figure 4g) compared to the clear-sky simulation (Figure 1d) to <1 ppbv for four models and introduces O_3 loss in the CAPRAM of 3–4 ppbv. The model predicted O_3, especially by the CAPRAM model, matches observations well.

The ratios of the gas-phase mixing ratio to the total (gas + aqueous) mixing ratio can be compared among models. First, the aqueous phase concentration is converted to a mixing ratio ($C_a = X_a \cdot q_c \cdot MW_{air} \cdot 1 \times 10^{-6}$ where C_a is aqueous-phase mixing ratio [mol oxidant mol^{-1} air], X_a is aqueous phase concentration [mol X L^{-1} H_2O], q_c is cloud water mass mixing ratio [g H_2O kg^{-1} air], MW_{air} is molecular weight of air [28.966 g mol^{-1}], and 1×10^{-6} converts units). The total mixing ratio is the sum of the gas-phase and aqueous-phase mixing ratios. Comparing the gas-phase mixing ratios of the oxidants to their total mixing ratios at hour 19 (nighttime), the five models tend to agree with respect to partitioning between gas and aqueous phases in that OH and O_3 are approximately completely in the gas phase (>99.9%), HO_2 is nearly all in the gas phase (>80%), and only ~20% of the H_2O_2 is in the gas-phase. Partitioning of trace gases is discussed in more detail below.

Aqueous-phase oxidant concentrations (right column of Figure 4) vary among the models. At night, OH concentrations range from 5×10^{-15} to 12×10^{-15} M, while at midday aqueous-phase OH ranges from 1×10^{-13} to 50×10^{-13} M, with the GAMMA and CLEPS models predicting higher OH than the CAPRAM and Barth models and the Ervens model predicting less daytime OH. At night, the OH (aq) variability is

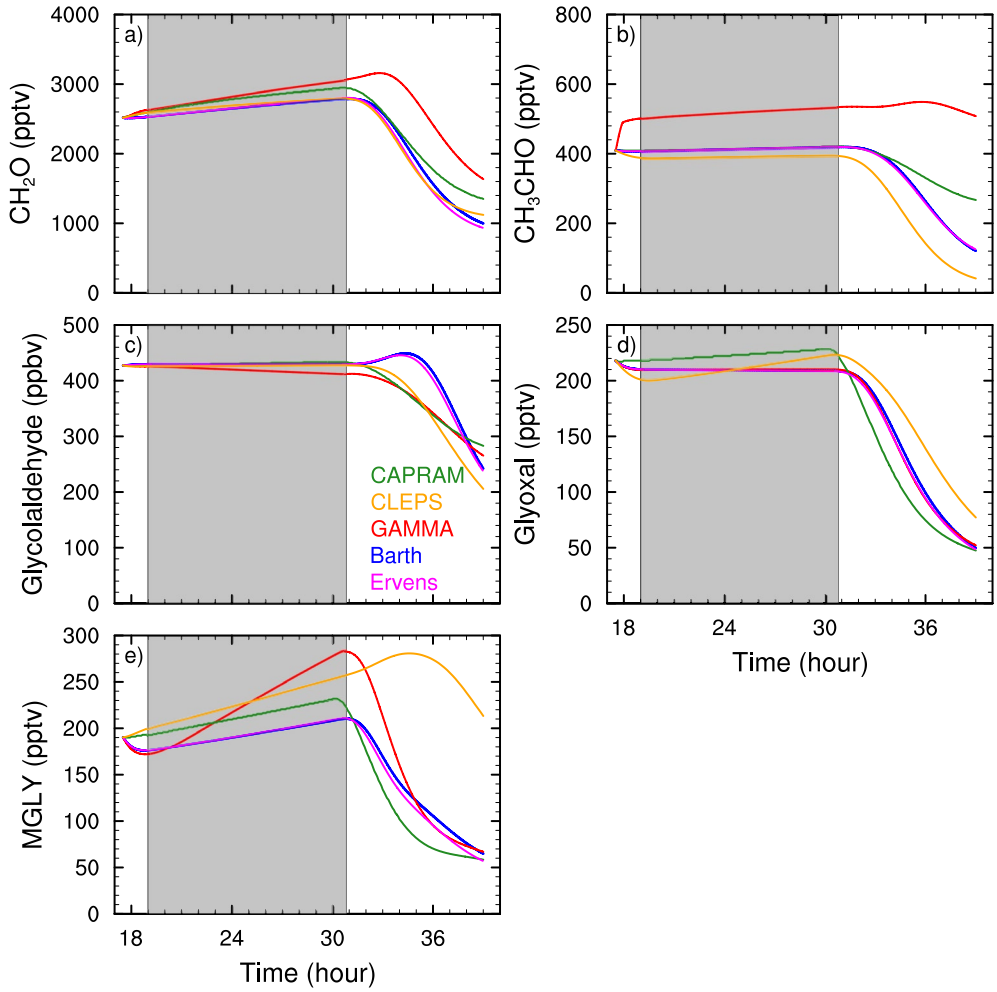

Figure 2. Time series of (a) Formaldehyde, (b) Acetaldehyde, (c) Glycolaldehyde, (d) Glyoxal, and (e) Methylglyoxal (MGLY) from the clear-sky only simulation. Results are colored by different models, where green lines are CAPRAM, gold lines are CLEPS, red lines are GAMMA, blue lines are Barth, and magenta lines are Ervens models. The gray shaded region denotes nighttime.

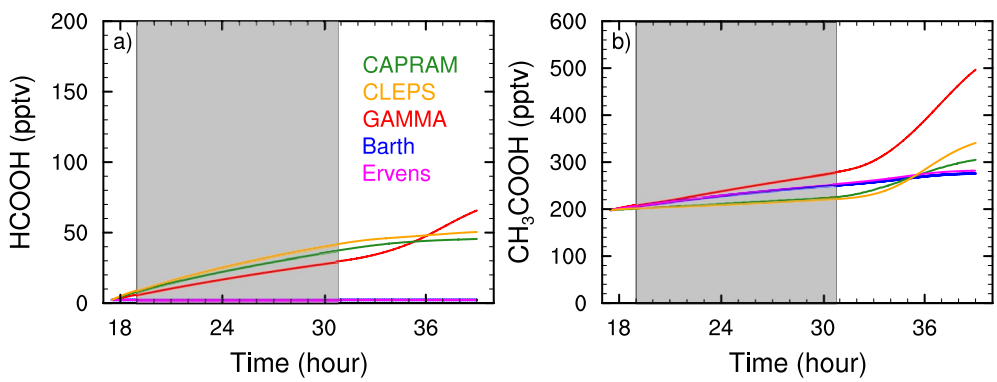

Figure 3. Time series of (a) Formic acid and (b) Acetic acid from the clear-sky simulation. Results are colored by different models, where green lines are CAPRAM, gold lines are CLEPS, red lines are GAMMA, blue lines are Barth, and magenta lines are Ervens models. The gray shaded region denotes nighttime.

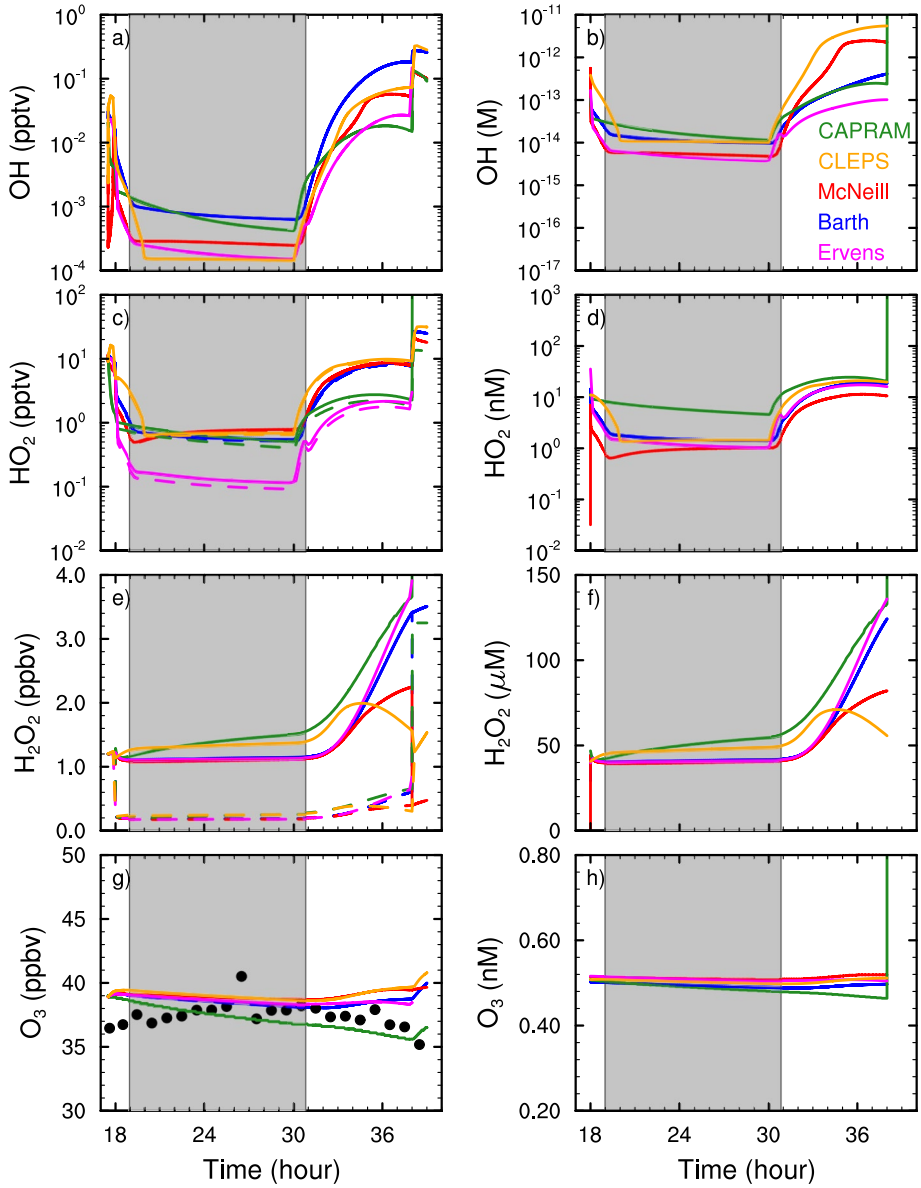

Figure 4. Time series plots from the cloud simulation with prescribed LWC and pH. Left column: Gas-phase and total (gas + aqueous phase) mixing ratios (dashed and solid lines, respectively); right column: corresponding aqueous-phase concentrations of the same species. (a, b) OH, (c, d), HO_2, (e, f) H_2O_2, and (g, h) O_3. Results are colored by different models, where green lines are CAPRAM, gold lines are CLEPS, red lines are GAMMA, blue lines are Barth, and magenta lines are Ervens models. The gray shaded region denotes nighttime. The black dots in the O_3 panel are hourly average observations from the WFM Summit Observatory measured by ASRC.

due to the different OH H_{eff} values (Table 3), such as the higher OH H_{eff} used by CLEPS which increases the gas to aqueous phase transfer of OH, as well as differences in aqueous-phase reaction rates (Table 4) affecting OH (aq) concentrations. During daytime, the CLEPS OH (aq) is also affected by using different photolysis rate constants than the other models (Figure S2 in Supporting Information S2). Aqueous-phase HO_2 concentrations are similar among four of the five models with CAPRAM predicting much higher HO_2 at night. All models predict nighttime aqueous-phase H_2O_2 concentrations to be mostly constant (although H_2O_2 shows a $\sim 1 \times 10^{-5}$ M increase in CAPRAM). During daytime, all models predict an increase in H_2O_2 aqueous-phase concentrations, although the CLEPS model displays a decrease in aqueous H_2O_2 after hour 33 hr due to the H_2O_2 (aq) + OH (aq) reaction, which becomes dominant for the elevated OH concentration.

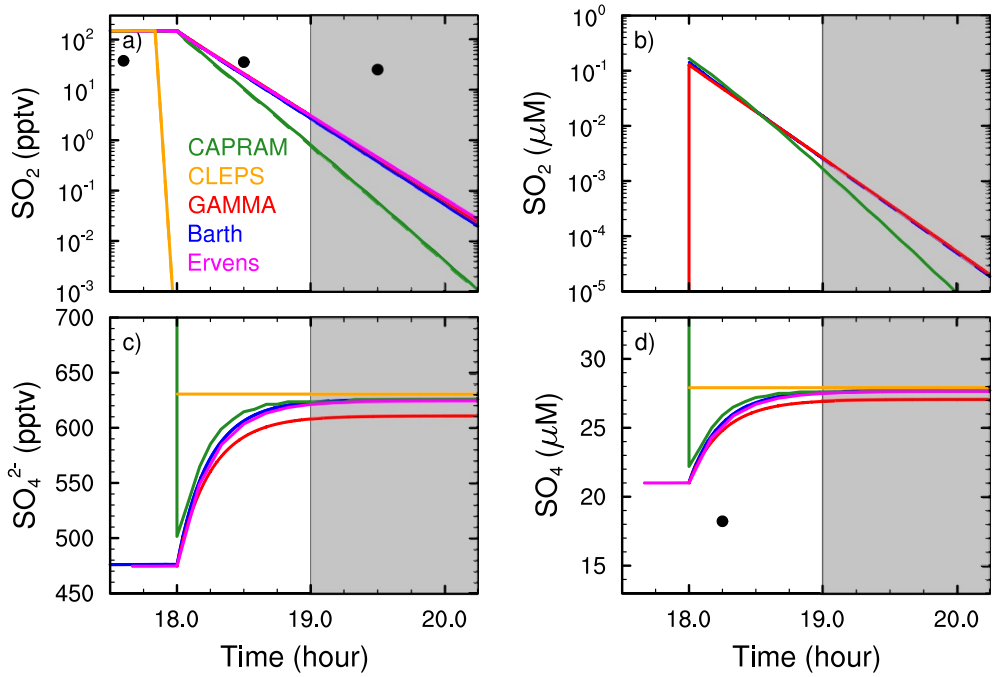

Figure 5. Same as Figure 4 but for (a, b) SO_2 and (c, d) SO_4^{2-} and for the first ~3 h of the simulation. Total S(IV) is dominated by its gas-phase mixing ratio, while total S(VI) is entirely in the cloud water. Thus, only total SO_2 and SO_4^{2-} are visible in panels (a) and (c). The gray shaded region denotes nighttime. The black dots in panel (a) are hourly observations and in panel (d) are from the first 12-hourly cloud water sample from WFM Summit Observatory provided by ALSC.

The temporal trend in H_2O_2 is due to the availability of aqueous-phase OH and HO_2. Aqueous-phase O_3 concentrations predicted by the different models are quite similar.

The oxidation of S(IV) in the aqueous phase to form sulfate goes to completion within the first hour or so of the onset of cloud (Figure 5). The Barth, GAMMA, and Ervens models represent the SO_2 depletion on the same timescale (overlapping lines in Figures 5a and 5b), while the CAPRAM model depletes SO_2 somewhat more rapidly and the CLEPS model depletes SO_2 immediately, because the high OH (aq) concentrations predicted by CLEPS oxidize S(IV) rapidly during the first hour of cloud, which is still in daylight. Three models conserve $SO_2 + SO_4^{2-}$, which is initially 626 pptv. Observed gas-phase SO_2 maintains near-constant values during the time period, indicating a source (likely from transport) to the WFM Observatory that is not included in the configuration of the box model simulations. While adding a source of SO_2 (or other trace gases) from transport or mixing may create a more realistic simulation, the lack of such a source does not distract from the goal of the paper which is to evaluate the similarities and differences of five gas-aqueous chemistry models including their reaction mechanisms.

Major inorganic ion concentrations predicted by the models can be compared to the measurements taken by the ALSC for the cloud event (Table 5). Note that these measurements were not available at the time the box model simulations were configured. The box model initialization was based on output from a WRF-Chem simulation (Section 3), which predicted low ammonium (NH_4^+) concentrations likely because of low NH_3 emissions. Thus, box model predictions of NH_4^+ concentrations are much lower than those measured. However, if the box model initial NH_3 mixing ratios were increased to 1 ppbv, the predicted NH_4^+ concentration would be in line with observations (as found by the Barth model for the 06:00 LT September 18, 2016 comparison). Sulfate concentrations are overpredicted by the box models, which is caused by SO_2 initial mixing ratios being 2–3 times greater than observations (Figure 5). Modeled nitrate concentrations are low at the beginning of the cloud event because nitrate aerosol was not included in the model initialization, but nitrate concentrations agree within ±2 μM for the 06:00 LT September 18, 2016 comparison time for five of the six models. This good agreement in NO_3^- is likely due to initializing the box models with measured

Table 5
Initial Conditions and Concentrations of Cloud Water Inorganic Ions From ALSC Measurements and Model Predictions

	NH_4^+ (μmol/L)	SO_4^{2-} (μmol/L)	NO_3^- (μmol/L)
Initial conditions from WRF-Chem	7.16	21.066	0
September 17, 2016 at 18:00 LT			
ALSC measurements	47.64	18.22	24.70
CAPRAM	7.16	27.20	18.40
CLEPS	7.16	27.91	18.19
GAMMA	7.16	26.18	18.27
Barth (18:30 LT)	7.16	26.83	17.71
pH = 5.1 results	7.16	27.12	17.71
Ervens	7.16	26.71	17.78
September 18, 2016 at 06:00 LT			
ALSC measurements	33.27	13.24	21.44
CAPRAM	7.16	27.70	28.80
CLEPS	7.16	27.91	23.03
GAMMA	7.16	27.04	23.59
Barth (06:00 LT)	7.16	27.70	21.04
pH = 5.1 results	7.16	27.70	20.90
Vary pH, add 1000 pptv NH_3 (pH = 4.45)	44.00	27.73	21.04
Ervens	7.16	27.63	22.46

NO and NO_2 (Section 3) and nighttime conditions when the loss of NO_x is negligible due to low OH concentrations.

The onset of cloud introduces substantial differences in aldehyde mixing ratios among the box models (Figure 6). All models have CH_2O total mixing ratios showing a 0–500 pptv increase during nighttime followed by a 1000–1700 pptv decrease in CH_2O total mixing ratios during daylight when CH_2O oxidation by OH in both gas and aqueous phases and gas-phase photolysis of CH_2O are prevalent. Noting the logarithmic scale, aqueous-phase CH_2O concentrations range from 1 to 35 μM at night and 0.02–15 μM at midday. The GAMMA model does not include aqueous-phase oxidation of CH_2O, thus the minor depletion seen in aqueous CH_2O during day is due to equilibrating with lower gas-phase CH_2O concentrations. The lower aqueous-phase CH_2O concentrations from the CLEPS model are due to the elevated OH (aq) concentration causing a substantial depletion of aqueous CH_2O. There are also differences in partitioning between gas and aqueous phases among the models, with the CLEPS model showing CH_2O nearly 100% in the gas phase and the other three models showing 70%–85% of total CH_2O in the gas phase.

Modeled acetaldehyde (Figures 6c and 6d) varies among models, with the GAMMA model predicting ~100 pptv more acetaldehyde than the other models due to gas-phase chemistry (Figure 2), and photochemistry affecting predictions during daytime. Because of its low H_{eff} value (30 M atm^{-1}), acetaldehyde is nearly completely in the gas phase, thus only the total mixing ratios are seen in Figure 6c. The total acetaldehyde mixing ratios are quite similar to the clear-sky-only simulation 1 (Figure 2b) except for the CAPRAM model results, which, instead of decreasing acetaldehyde during daytime, shows a small increase in total acetaldehyde mixing ratio (Figure 6c) because of gas-phase oxidation of propene and photolysis of 3-hydroxy-2-methylpropanal which compensate for the loss rates in the aqueous phase. In the aqueous phase, the CLEPS, Barth, and Ervens models show a depletion during daytime in acetaldehyde due to reduced gas-to-drop transfer with the lower gas-phase mixing ratios. The Ervens model predicts a lower aqueous acetaldehyde concentration because of the lower H_{eff} value (11.4 M atm^{-1}) employed in that model compared to the other models. A decrease in aqueous acetaldehyde is not seen in the CAPRAM model results or GAMMA model results because their gas-phase mixing ratios did not decrease substantially.

Glycolaldehyde gas-phase mixing ratios and aqueous concentrations differ among models (Figures 6e and 6f), in contrast to Simulation 1 which show strong agreement among models during night and similar behavior for three of the models during daylight. With its high H_{eff} value (70,000–80,000 M atm^{-1}) and high aqueous-phase oxidation rate constant with OH (>10^9 M^{-1} s^{-1}), glycolaldehyde is controlled mostly by the aqueous-phase chemistry. In the aqueous phase during daylight, there is substantial depletion of aqueous glycolaldehyde in the CLEPS and GAMMA models, moderate depletion in the CAPRAM and Barth models, and a small increase in aqueous glycolaldehyde in the Ervens model. These differences are not simply explained by differences in the H_{eff} value or reaction rate constant of aqueous glycolaldehyde with OH, but are likely because the OH (aq) concentration differs among models (Figure 4b). For example, OH (aq) is highest in the CLEPS and GAMMA models allowing more aqueous glycolaldehyde depletion.

Glyoxal total mixing ratios also vary among models, with mixing ratios ranging from 140 to 200 pptv at night and 0 to 50 pptv at midday, but show the same general trend of small depletion during nighttime and a large depletion during daylight. Because a large depletion of glyoxal is found with gas-phase only chemistry during daylight (Figure 2d), the aqueous-phase glyoxal oxidation mostly enhances the total depletion. All of the models use the same H_{eff} values (1.2×10^6 M atm^{-1}) and aqueous-phase reaction rate constants are

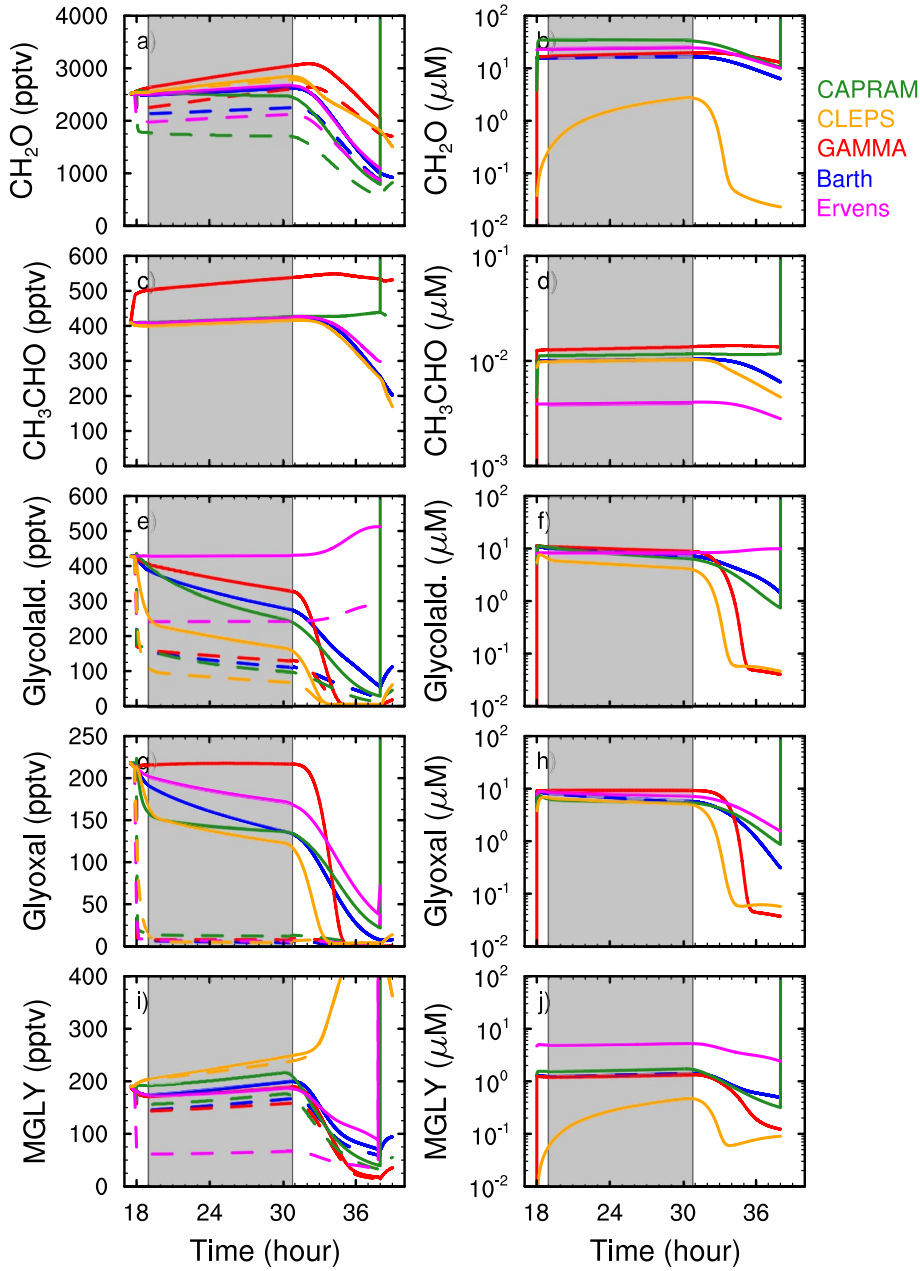

Figure 6. Same as in Figure 4 but for (a, b) CH_2O, (c, d) CH_3CHO, (e, f) glycolaldehyde, (g, h) glyoxal, and (i, j) methylglyoxal.

within a factor of two. Thus, differences found among models are because of the differences in the predicted OH (aq) concentration.

Methylglyoxal total mixing ratios are fairly similar among the models and show similar temporal trends during nighttime, but are quite different during daytime, when the CLEPS model predicts increasing MGLY while the other models predict decreasing mixing ratios. The gas-phase only simulation (Figure 2e) shows increases in MGLY during night for all models, and most substantially in the GAMMA and CLEPS models. MGLY in the gas-phase only CLEPS model simulation continues to increase during daylight until 11 a.m. (35 hr). Thus, the increase in total MGLY during daylight in the CLEPS gas-aqueous chemistry simulation could also be due to the gas-phase chemistry scheme used by that model. Aqueous-phase MGLY concentrations have similar trends among the other five models with fairly constant values at night and a decrease in

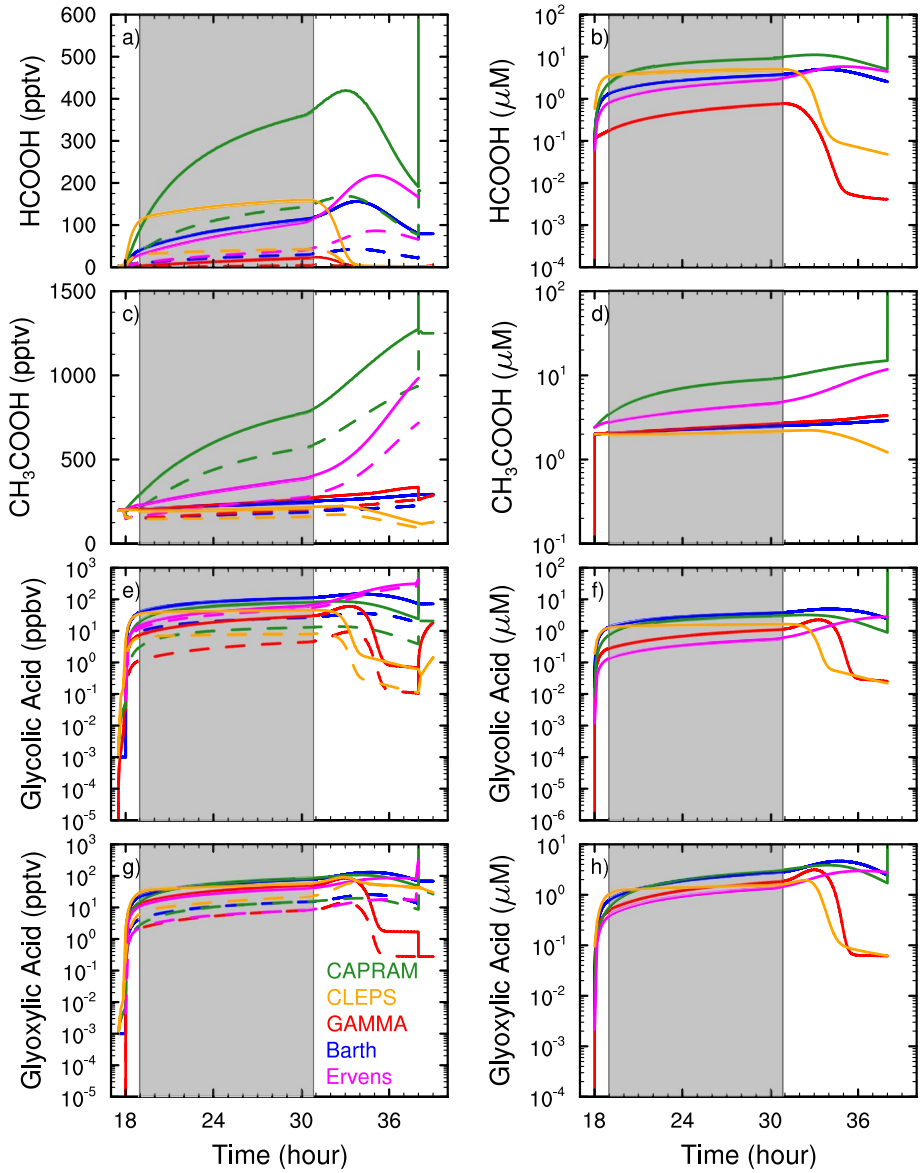

Figure 7. Same as Figure 4 but for (a, b) formic acid, (c, d) acetic acid, (e, f) glycolic acid, and (g, h) glyoxylic acid.

concentration during the day, but its concentration varies by an order of magnitude among the five models and reflects the different H_{eff} constants used by the models (Table 3) and the elevated OH (aq) concentration increasing MGLY (aq) destruction in the CLEPS model.

Due to the variability among models for both the aldehydes and OH radical, the variability among models for the organic acids (Figure 7) is also quite substantial. Formic acid production in the aqueous phase occurs during nighttime in all the models until 1–4 hr after sunrise depending on the model. However, the formic acid production magnitude varies greatly among the models. The CAPRAM model produces >400 pptv total formic acid while the GAMMA model produces 50 pptv total formic acid because the GAMMA model does not include aqueous CH_2O oxidation by OH. The high HCOOH production in CAPRAM is due to the high CH_2O (aq) and OH (aq) concentrations in CAPRAM at night. In addition, CAPRAM and CLEPS models include HCOOH (g) production at night from ozone reaction of ethene or other unsaturated compounds. The effect of excluding aqueous-phase CH_2O oxidation in the GAMMA model increases the OH (aq) concentration and therefore reduces organic acid concentrations during daytime more quickly than if aqueous CH_2O oxidation were included (Figure S3 in Supporting Information S2). However, by the end of the simulation,

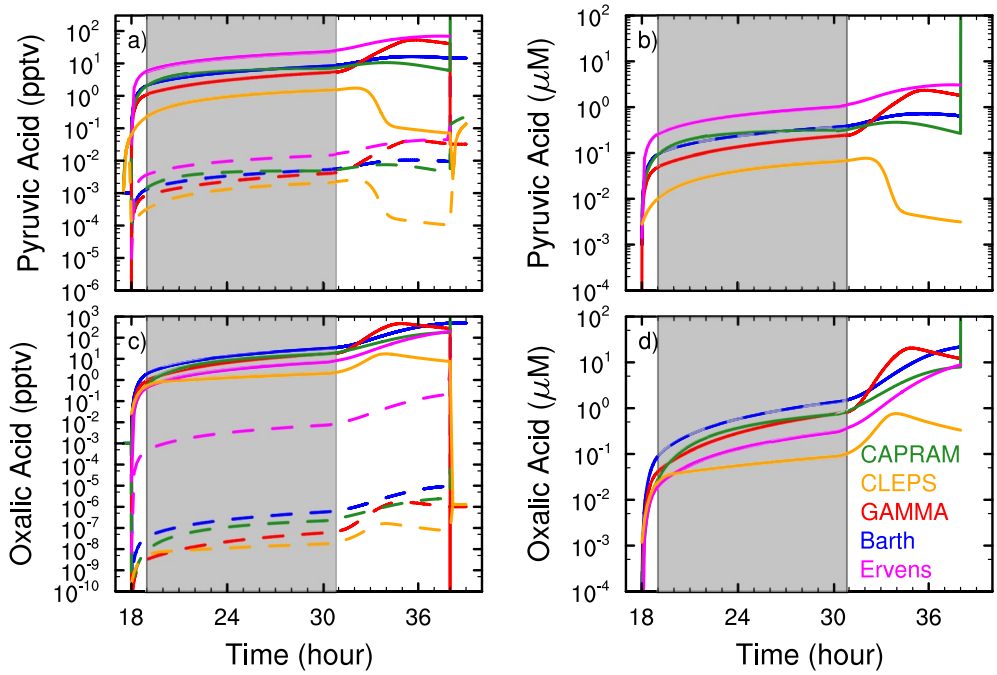

Figure 8. Same as Figure 4 but for (a, b) pyruvic acid and (c, d) oxalic acid.

the organic acid concentrations are nearly the same for a GAMMA sensitivity simulation where aqueous CH_2O oxidation was included (Figures S4 and S5 in Supporting Information S2). Due to its oxidation by OH in the aqueous phase, HCOOH decreases during most of the day depending on the OH concentration.

Predictions of total acetic acid mixing ratios (Figures 7c and 7d) are similar among three models (GAMMA, Barth, and CLEPS) showing rather constant mixing ratios at night and changes of ±100 pptv during the day. The CAPRAM and Ervens models predict large increases (800–1000 pptv) in total acetic acid, because these two models include aqueous-phase acetyl peroxy radical (CH_3CO_3) reacting with O_2^-, which produces peracetic acid and acetate in the CAPRAM and Ervens models, respectively. In the CAPRAM model, peracetic acid reacts with bisulfite ion to form acetic acid. In CAPRAM, acetyl peroxy radical can also undergo hydrolysis, which leads to acetic acid formation (Tilgner et al., 2013), and pyruvic acid aqueous-phase reaction with H_2O_2 produces acetic acid. The acetyl peroxy radical hydrolysis pathway is the dominant source of acetic acid for the simulated conditions. While the CLEPS model includes aqueous-phase $CH_3CO_3 + O_2^-$ to form peracetic acid, the peracetic acid reacts only with sulfite ion, which has a small concentration at pH = 4.5. The CLEPS model also includes reaction between pyruvic acid and H_2O_2, but it is a small source of acetic acid for the simulated conditions.

Total mixing ratios of glycolic and glyoxylic acids vary by two orders of magnitude among the models (Figures 7e–7h), but the five models predict a similar trend with a small increase during the cloud event. The CLEPS and GAMMA models show an order of magnitude decrease in daytime when the aqueous-phase OH in these two models increases substantially (Figure 4b). The exclusion of the aqueous CH_2O oxidation in the GAMMA model causes this decrease to occur earlier in the day, but organic acid concentrations at the end of the simulation are the same (Figures S4 and S5 in Supporting Information S2).

Pyruvic acid total mixing ratios (Figures 8a and 8b) vary by 1–2 orders of magnitude among models, but show the same general trend of increasing mixing ratios during the night and early morning. The higher pyruvic acid mixing ratios from the Ervens model occurs because of the high MGLY H_{eff} value used by that model (9.3×10^4 M atm^{-1} compared to 1.1×10^4 M atm^{-1} by the other models, Table 3). The lower pyruvic acid mixing ratios predicted by the CLEPS model is due to the combination of aqueous-phase photolysis of pyruvic acid and the lower pyruvic acid H_{eff} value used by that model (3.5×10^7 M atm^{-1} compared to 7.2–8.3×10^7 M atm^{-1} by the other models) together with lower concentration of pyruvic acid in the gas phase. The oxidation of pyruvic acid in the aqueous phase is more efficient due to the high OH (aq) concentration

and pyruvic acid loss by photolysis and its reaction with H_2O_2, which may not be considered in all of the other models.

Oxalic acid production at night ranges from 1 to 20 pptv for the total mixing ratio predicted by all of the models. Total oxalic acid production continues during daytime with midday mixing ratios of 10–500 pptv, potentially contributing 0.03–1.6 μg m^{-3} to aerosol formation. Since oxalic acid formation relies on both its own and its precursor H_{eff} values and reaction rate constants, the variation in oxalic acid concentrations is not surprising. Finding a large range of oxalic acid production among the models has implications on how well the community can predict aqueous SOA formation from cloud chemistry (Ervens et al., 2011). The results shown here point to the need for reliable H_{eff} and reaction rate constants, as some of the variation among model results is due to different values used for these coefficients. It should also be noted that oxalate forms salts and complexes in the aqueous phase which is not accounted for by Henry's law. Thus, the assumption of complete partitioning of oxalic acid to the aqueous phase appears to be justified.

While the Barth and Ervens models predict only the production of the 6 acids already discussed, the CLEPS, CAPRAM, and GAMMA model also include C3 and C4 organic acids, such as malonic and succinic acids. In the CLEPS model, the sum of HCOOH, CH_3COOH, glycolic, glyoxylic, pyruvic, and oxalic acids is 90% or less of the total aqueous organic acids, where 2-hydroxyperacetic acid, 2-hydroxyperoxy acetic acid, performic acid, and peracetic acid are the main contributors to the remaining total acid. The CLEPS model predicts 5.6–13.8 μM of total aqueous organic acid, while the sum of aqueous HCOOH, CH_3COOH, glycolic, glyoxylic, pyruvic, and oxalic acids ranges from 1.8 to 10.6 μM (Figure 9a). These concentrations are similar to the GAMMA, Barth and Ervens models especially at night, but are smaller than that predicted by the CAPRAM model.

TOC concentrations measured by ALSC ranged from 112 to 404 μM for three samples obtained September 17–18 (and 247 μM for a composite sample with all three samples combined), while DOC measured by Herckes was 222 μM and WSOC measured by Weber was 298–309 μM from aliquots of the composite sample. The model organic carbon can be estimated from the organic carbon in the nucleating aerosol and the sum of the organic acids. Initial OC in PM2.5 was 0.52 μg kg^{-1} (see Supporting Information S1), which is equal to 55 μM. At $t = 30$ h, the sum of the aqueous-phase organic acids ranges from 2 to 26 μM (Figure 9a). Thus, the modeled OC ranges from 57 to 81 μM, which is 2–6 times less than observed. Carbonyls could also contribute to OC (Herckes et al., 2013). When including carbonyls (Figure 6), the modeled OC ranges from 80 to 110 μM, which is still much smaller than observed. Discrepancies between observations and model are likely due to the low initial OC aerosol concentrations taken from the WRF-Chem simulation, in which chemical transformations in aerosols were inadvertently omitted. It should also be noted that a large fraction (35%–85%) of the organic content in cloud and fog water is usually not characterized on a molecular level (Dominutti et al., 2021; Herckes et al., 2013). Therefore, its formation processes cannot be included in models.

Much of the sum of organic acids (Figure 9a) increase predicted by CAPRAM is from the increase in aqueous-phase formic and acetic acids (Figure 7), while the organic acid production predicted by the Ervens model is primarily from acetic acid production, and from formic, acetic, and glycolic acids in the Barth model. In contrast, much of the increase of total organic acids predicted by the GAMMA model is from the increase in oxalic acid (Figure 8). In a sensitivity simulation conducted by the GAMMA model, the contribution from the individual organic acids to the total organic acid concentration is consistent with the results shown in Figure 8.

Partitioning among the six main organic acids (HCOOH, CH_3COOH, glycolic, glyoxylic, pyruvic, and oxalic acids) in the aqueous phase varies between the models (Figures 9b–9f). Both the Barth and Ervens models predict similar trends for the partitioning among species, for example, CH_3COOH is the primary organic acid early on but quickly decreases as the fraction contribution and oxalic acid fraction contribution increases substantially during daytime. However, the magnitude of the individual organic acid contributions to total organic acids varies because of differences of Henry's law constants (Table 3, e.g., MGLY, HCOOH, and glycolic acid) and small differences in aqueous oxidation reaction rate constants (Table 4). The CAPRAM, CLEPS, and GAMMA models also predict high acetic acid fraction early with a rapid decrease. CAPRAM and CLEPS models show significant fraction of HCOOH at night that is not seen in the GAMMA model

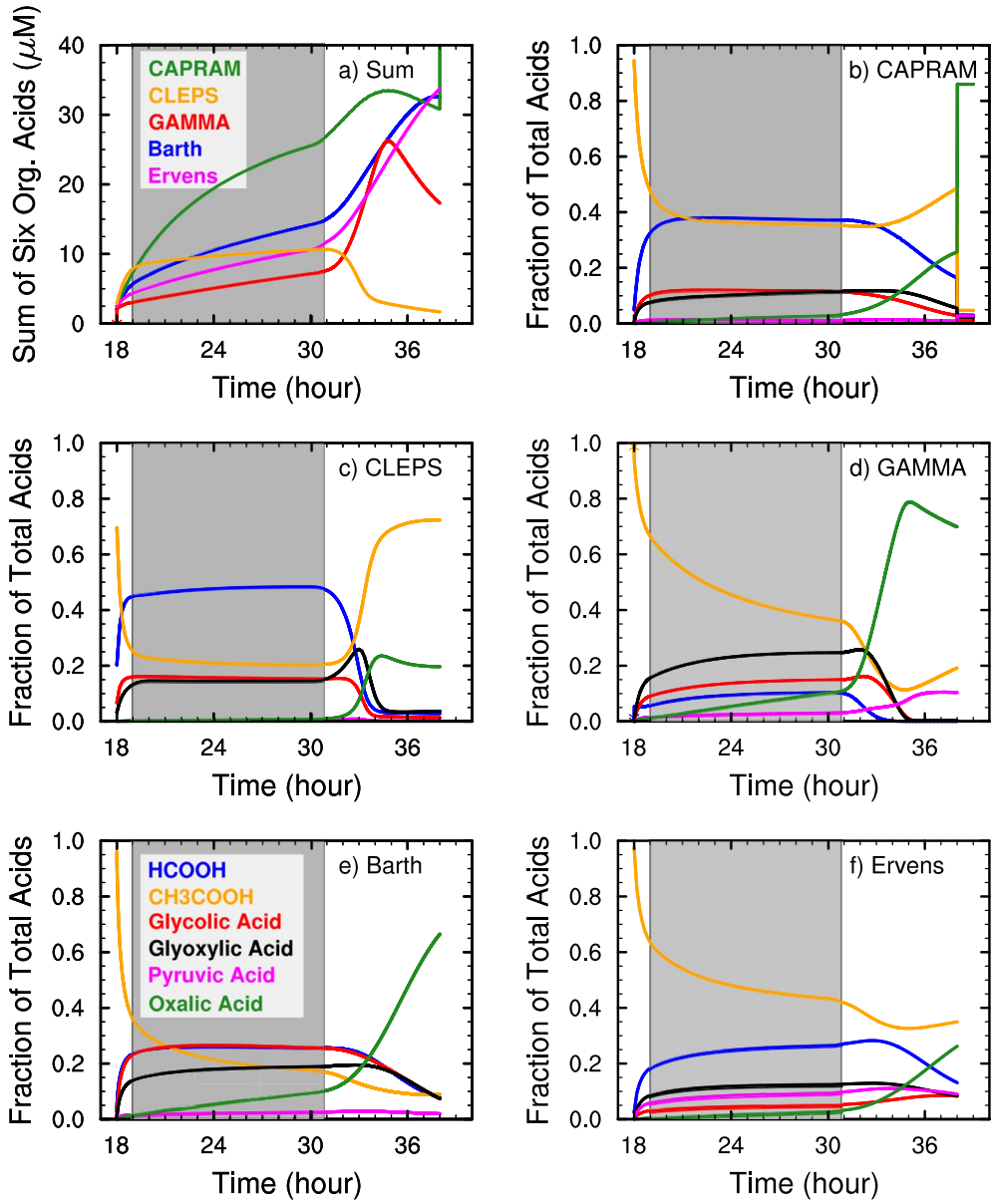

Figure 9. Time series from the cloud simulation with prescribed LWC and pH of (a) Sum of aqueous-phase HCOOH, CH_3COOH, glycolic, glyoxylic, pyruvic, and oxalic acids, and (b–f) Fraction of individual aqueous-phase organic acids of the sum shown in (a). Results in panel (a) is colored by different models, where green is CAPRAM, gold is CLEPS, red is GAMMA, blue is Barth, and magenta is Ervens model. Results in panels (b–f) are colored by different organic acids, where blue is HCOOH, gold is CH_3COOH, red is glycolic acid, black is glyoxylic acid, magenta is pyruvic acid, and green is oxalic acid. The gray shaded region denotes nighttime.

results because of the lower OH (aq) concentrations in GAMMA at night (Figure 4b) compared to CAPRAM and CLEPS and lack of aqueous-phase oxidation of CH_2O in the GAMMA model. The fraction of oxalic acid varies among all the models with GAMMA and Barth models showing oxalic acid as the main organic acid at midday (t = 36 hr) for these six organic acids, while the other models have oxalic acid fraction near 0.2.

The partitioning factor, q_{part}, signifies whether a trace gas is in thermodynamic equilibrium as described by the Henry's Law constant. The partitioning factor is defined as (e.g., Audiffren et al., 1998; Rose et al., 2018)

$$q_{\text{part}} = \frac{C_a}{H_{\text{eff}}\, R\, T\, q_{\text{cw}}\, C_{\text{g}}}$$

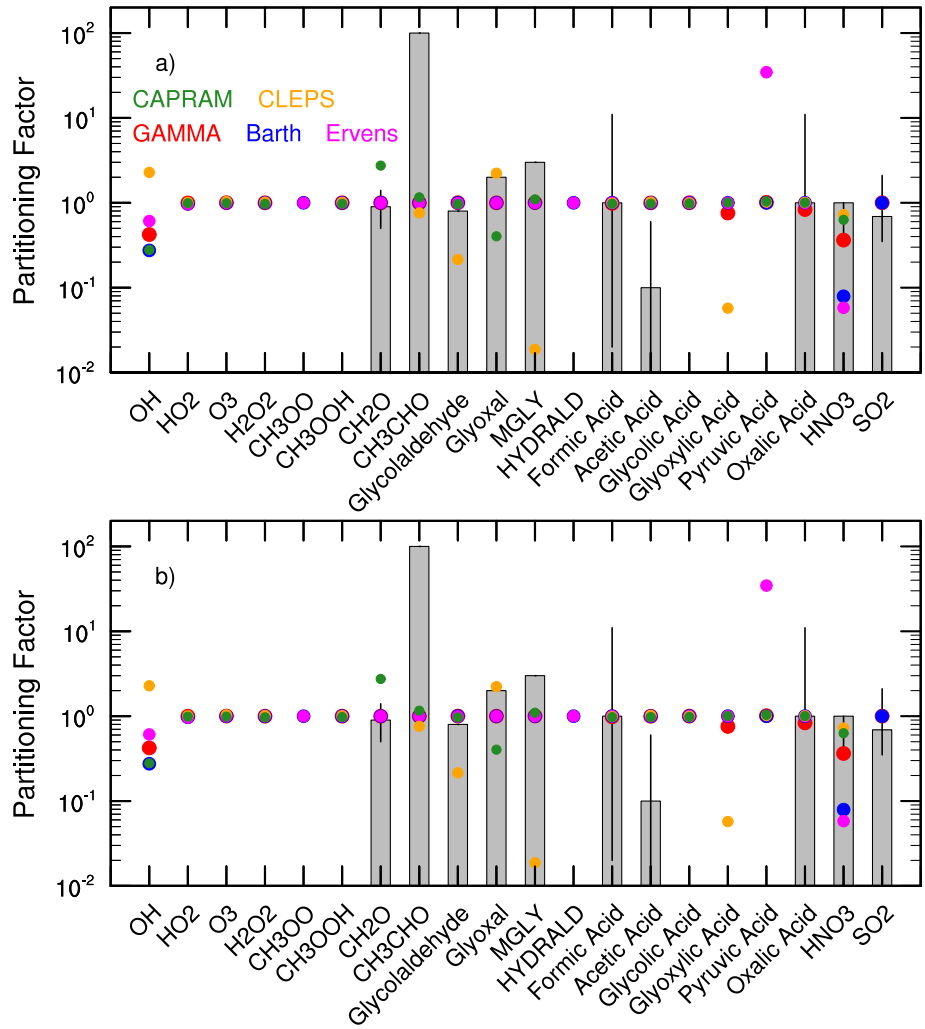

Figure 10. Partitioning factor q_{part} (dimensionless) for key aqueous-phase oxidants and acids at (top) t = 19 hr, 1 hr after cloud onset and (bottom) t = 36 hr, 18 hr after cloud onset from the cloud simulation with prescribed LWC and pH. The species is in Henry's Law equilibrium when $q_{part} = 1$. Modeled SO_2 $q_{part} = 0$ at t = 36 hr because SO_2 is depleted. Results are colored by different models, where green circles are from CAPRAM, gold circles are CLEPS, red circles are GAMMA, blue circles are Barth, and magenta circles are Ervens models. The gray boxes and black lines are derived partitioning factors from observations in previous field studies. References are van Pinxteren et al. (2005) for CH_3CHO, glyoxal, methylglyoxal, and glycolaldehyde; S.-M. Li et al. (2008) for CH_2O; Winiwarter et al. (1994) and Munger et al. (1989) for formic and acetic acids; Sellegri et al. (2003) for oxalic and nitric acids; and Voisin et al. (2000) for SO_2, and are taken from Ervens (2015).

where C_a and C_g are the aqueous-phase and gas-phase volume mixing ratios, H_{eff} the effective Henry's Law constant (M atm^{-1}), R the ideal gas constant (0.08206 atm L mol^{-1} K^{-1}), T temperature (K), and q_{cw} the liquid water content (L H_2O (L air) $^{-1}$). When $q_{part} = 1$, the trace gas is in Henry's Law equilibrium. For $q_{part} > 1$ and $q_{part} < 1$, the trace gas is supersaturated and subsaturated, respectively.

A comparison of the partitioning factor among the five models and from derivations of observed partitioning is presented in Figure 10 using model results at t = 19 h and t = 36 h. Most model-derived partitioning factors are constant with time, especially at night. During daytime, more variation is found particularly for highly reactive OH and highly soluble HNO_3 as discussed below. The derived observations, which are summarized in Ervens (2015), are from various field studies in the northern midlatitudes. Those listed studies together with other recent ones exhibit some deviations from the thermodynamic equilibrium, especially supersaturations for less soluble organics (van Pinxteren et al., 2005; Wang et al., 2020). For all models, most trace gases are predicted to be in Henry's law equilibrium. These agree with derived partitioning factors

from observations except for CH_3CHO and acetic acid. Observations from two different field campaigns suggest CH_3CHO is supersaturated while acetic acid is subsaturated. Trace gases that are not predicted to be in Henry's Law equilibrium include OH, CH_2O, glyoxal, methylglyoxal, pyruvic acid, glyoxylic acid, HNO_3, and SO_2. The high chemical reactivity of OH often prevents OH from reaching equilibrium, with four models showing OH (aq) to be subsaturated. However, the CLEPS model shows OH is supersaturated in the cloud water, possibly from aqueous-phase chemical production.

The high solubility of HNO_3 often prevents it from reaching equilibrium. At t = 19 h, three models show HNO_3 to be subsaturated in the aqueous phase, but the CLEPS model has HNO_3 in equilibrium and the CAPRAM model has HNO_3 slightly supersaturated. At t = 36 h, HNO_3 is subsaturated in all models; the GAMMA and Barth models HNO_3 partitioning factors are 0.002 and 0.003, respectively. In some cases, rapid aqueous chemistry can result in the aqueous-phase trace gas to be supersaturated. For example, in the Ervens model, the high H_{eff} for methylglyoxal coupled with fast oxidation by OH (aq) causes pyruvic acid to be supersaturated (Figure 10) for both night and daytime conditions.

An analysis of the OH (aq) sources and sinks provides insight on some of the reasons why organic acid production differs among models. The reaction of O_3 and O_2^- in the aqueous phase is a primary source of OH (aq), especially at night (note that there is no Fenton chemistry included in this simulation). The $O_3 + O_2^-$ reaction is sensitive to the Henry's law constant of HO_2 and its dissociation constant. Thus, the CAPRAM and Ervens models with their higher H_{eff} for HO_2 (Table 3) produce more OH (aq) than the other three models via this reaction. Other significant sources of OH (aq) during the middle of the day include aqueous-phase photolysis of H_2O_2 and the mass transfer of OH from the gas-phase, which depends on the OH H_{eff} (i.e., there is greater mass transfer into cloud water in the CLEPS model because of its higher H_{eff} than the CAPRAM, GAMMA, and Ervens models). The high OH (aq) concentrations in the CLEPS model during the daytime are a result of high production of OH in the gas phase from O_3 photolysis followed by mass transfer of OH. The OH (aq) sinks are more numerous and the dominant loss reactions vary depending on night or day chemistry. In general, reactions with CH_2O, glycolaldehyde, glyoxal, and HCOOH are the main sinks during nighttime, while reactions with these species, other organic acids, and H_2O_2 contribute to daytime OH (aq) losses. For these reactions, differences among models occur because of differences in H_{eff} for the organic species and their reaction rate constants.

The results of the clear-sky simulation (Section 4.1) showed that the Barth and Ervens models give very similar results. Therefore, differences in the results between these two models of the gas-aqueous chemistry simulation are due to phase transfer fluxes and associated constants used, that is the aqueous-phase reaction rate constants, and aqueous-phase chemistry mechanisms. Analysis of the OH (aq) sources and sinks at the initial time step of cloud encounter show where the most important differences occur. The higher HO_2 H_{eff} in the Ervens model produces more OH (aq) than in the Barth model via the $O_3 + O_2^-$ reaction, while the higher CH_2O and MGLY H_{eff} values in the Ervens model cause more OH (aq) destruction. In sum, the Ervens model has more OH (aq) production at its initial time step than destruction compared to the Barth model. These factors, coupled with other differences such as OH oxidation reaction rate constant of pyruvic acid and formation of acetic acid from the acetylperoxyl radical (ACO3), which is not included in the Barth model, contribute to the divergence of predicted aqueous-phase reaction rates by these two models. This analysis suggests that H_{eff} and aqueous reaction rate constants be reviewed by the community who can provide recommended values.

4.3. Sensitivity to Increased pH (Simulation 3)

As pH increases, the effective Henry's law constants increase, leading to more dissociation and a higher aqueous phase fraction (e.g., Andreae et al., 1988; Ervens, Herckes, et al., 2003; Winiwarter et al., 1994). In addition, the dissolved acid is present more as the anion than its protonated form (Seinfeld & Pandis, 2016). Further, aqueous-phase OH oxidation of the anion is much faster than that of the protonated form for most organic acids with less than five carbons. As an example, aqueous-phase OH oxidation of $HCOO^-$ is 25 times faster than that of HCOOH (Ervens, George, et al., 2003; Jacob, 1986; Tilgner et al., 2021). To learn how each model responds to a different pH, each group re-ran Simulation 2 using a pH value of 5.1. The pH = 5.1 value was chosen based on the measured pH by the Adirondack Lake Survey. Increasing pH from 4.5 to 5.1 decreased total HO_2 (Figure 11) in all five model results due to the higher effective Henry's Law

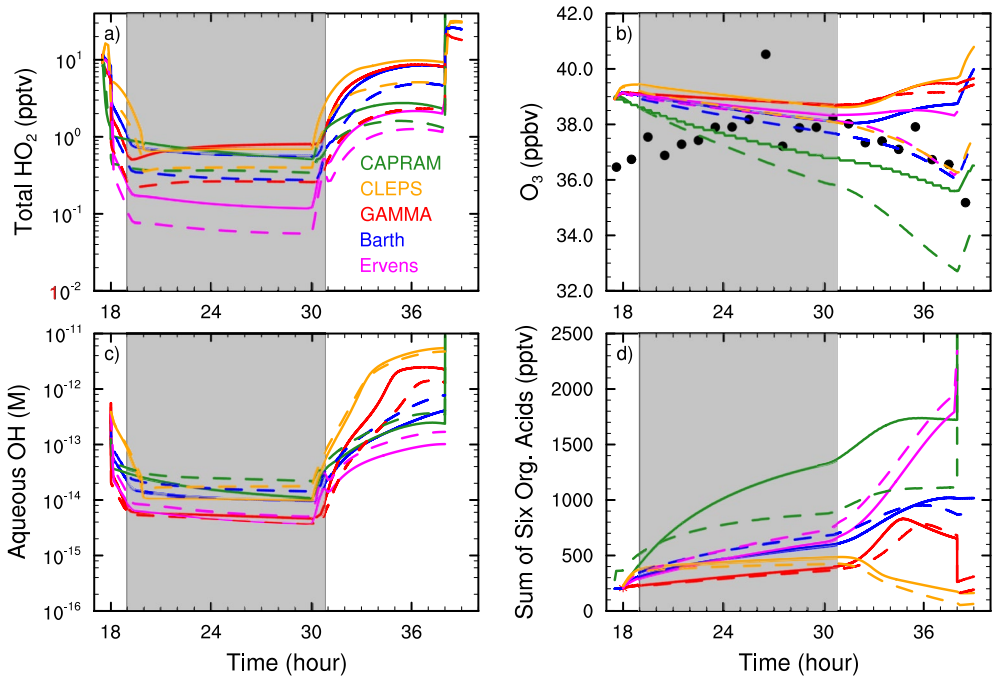

Figure 11. Time series with pH = 4.5 (solid lines) and pH = 5.1 (dashed lines) from Simulations 2 and 3 with prescribed LWC and pH of (a) total (gas + aqueous phases) HO_2 (pptv), (b) total O_3 (ppbv), (c) aqueous OH (M), and (d) total of all organic acids (pptv). Results are colored by different models, where green lines are CAPRAM, gold lines are CLEPS, red lines are GAMMA, blue lines are Barth, and magenta lines are Ervens models. The gray shaded region denotes nighttime. The black dots in the O_3 panel are hourly average observations from the WFM Summit Observatory measured by ASRC.

constants allowing more efficient dissociation of HO_2 in the aqueous phase. Superoxide (O_2^-) has a higher reactivity than HO_2, causing more total HO_2 depletion at pH = 5.1 compared to pH = 4.5. Total O_3 mixing ratios also decrease with the higher pH compared to the pH = 4.5 simulation, with more depletion occurring during daytime. The lower O_3 mixing ratios are again due to the faster rate of $O_3 + O_2^-$.

While all five models predict similar responses to total HO_2 and O_3, the response in aqueous OH and sum of formic, acetic, glycolic, glyoxylic, pyruvic, and oxalic acids differs among models. Aqueous-phase OH concentrations increase in the CAPRAM, Barth, and Ervens model simulations when pH is increased (Figure 11c). The CLEPS model shows an increase in aqueous-phase OH during nighttime, but predicts the same aqueous-phase OH concentration during daytime for both pH conditions. The GAMMA model predicts less aqueous-phase OH with pH = 5.1 than with pH = 4.5. With higher pH and increased aqueous-phase OH oxidation of acids, one would expect less aqueous-phase OH. However, aqueous-phase OH oxidation of aldehydes and organic acids produces HO_2, which allows for the $O_3 + O_2^-$ reaction to increase and produce OH. The increased rate of reaction of $O_3 + O_2^-$ is primarily responsible for aqueous OH production at nighttime, while aqueous-phase photolysis of H_2O_2 also contributes to OH production during daytime.

The higher aqueous-phase OH concentrations predicted in the pH = 5.1 simulation results in more oxidation in the cloud water, causing decreases in aqueous-phase aldehydes. Organic acids are both formed and destroyed by aqueous OH oxidation reactions. At higher pH, the increased oxidation of organic acids and carboxylates by both higher aqueous-phase OH concentrations and higher reaction rate constants for the anion, can result in lower organic acid concentrations at pH = 5.1 than at pH = 4.5. This response occurs throughout the simulation for the CAPRAM, CLEPS and GAMMA models (Figure 11d). However, the Ervens model predicts higher organic acid concentrations at pH = 5.1 than at pH = 4.5 during the entire simulation, and the Barth model predicts higher organic acid concentrations at nighttime and early morning but lower organic acid concentrations at midday. The higher organic acids at pH = 5.1 in the Barth and Ervens models are a result of the aldehydes concentrations (specifically CH_2O) remaining greater than the organic

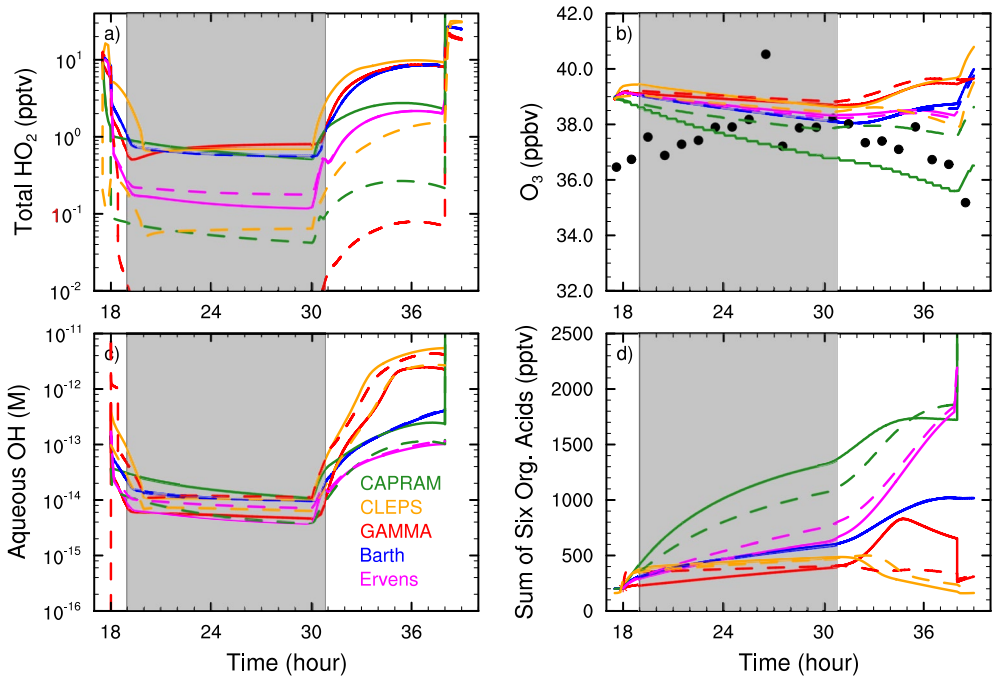

Figure 12. Time series with TMI chemistry (dashed lines) and without TMI chemistry (solid lines) from the cloud simulation with prescribed LWC and pH of (a) total (gas + aqueous phases) HO_2 (pptv), (b) total O_3 (ppbv), (c) aqueous OH (M), and (d) total of all organic acids (pptv). Results are colored by different models, where green lines are CAPRAM, gold lines are CLEPS, red lines are GAMMA, blue lines are Barth, and magenta lines are Ervens models. The gray shaded region denotes nighttime. The black dots in the O_3 panel are hourly average observations from the WFM Summit Observatory measured by ASRC.

acid concentrations, until oxalic acid formation produces concentrations that match or exceed CH_2O, at least in the Barth model.

4.4. Sensitivity to Presence of TMI (Simulation 4)

The control simulations were conducted without transition metal ion (TMI) chemistry, which can affect both the sulfate production directly (e.g., Deguillaume et al., 2004) and organic aqueous chemistry by forming complexes (Faust & Zepp, 1993; Long et al., 2013; Weller et al., 2014) and indirectly by forming OH radicals via Fenton and photo-Fenton chemistry. The aqueous chemistry mechanisms in all models except the Barth model include some TMI chemistry. Thus, just the model results from four models are examined to compare results with TMI chemistry.

Here, we show the impact of TMI chemistry on key oxidants and the formation of organic acids. Without data for the trace metal ions, their initial concentrations were set to averages of previous measurements at Whiteface Mountain (Siefert et al., 1998) using theoretical soluble fractions based on Deguillaume et al. (2005). This review emphasizes the fact that the soluble fraction is highly variable depending on the aerosol particle and often the water-soluble iron fraction is less important than those for manganese and copper. Although Siefert et al. (1996) determined soluble fractions for iron to be 22%–77%, in this study we follow Deguillaume et al. (2005), assuming the soluble fractions equal 5% for iron and 30% for manganese and copper. The initial TMI concentrations are listed in Table S5 in Supporting Information S3 with values ~0.02 μM for copper and ~0.05 μM for iron and manganese.

Simulation 4 with TMI chemistry is compared to Simulation 2 without TMI chemistry where both simulations have the same prescribed LWC and pH (Table 2). Three of the four models find that total (gas + aqueous phase) HO_2 mixing ratios decrease when TMI chemistry is included compared to aqueous chemistry without TMI chemistry (Figure 12). The CAPRAM and CLEPS total HO_2 decreases by an order of magnitude, while the GAMMA model decreases by ~2 orders of magnitude and the Ervens model shows a slight

increase in total HO_2 at night and no change during the day. Effects of TMI chemistry are small (<1 ppbv) for total O_3 mixing ratios (Figure 12b), with CAPRAM and GAMMA models predicting more O_3 and CLEPS and Ervens models predicting slightly less O_3. The aqueous OH concentrations are decreased by a factor of two in the CAPRAM and CLEPS model results compared to their no TMI chemistry results (CLEPS TMI results lie on top of the GAMMA no TMI results). The GAMMA model predicts more aqueous OH, and the Ervens model predicts little change in aqueous OH. The mixing ratios of the sum of formic, acetic, glycolic, glyoxylic, pyruvic, and oxalic acids change with the inclusion of TMI chemistry (Figure 12d). The CAPRAM model predicts less total organic acids with TMI chemistry than without, which is a result of less HCOOH production especially during night. With TMI chemistry, the HCOOH (total) mixing ratio in the CAPRAM model peaks an hour later than the simulation without TMI chemistry thereby reducing the HCOOH loss from OH oxidation. The GAMMA model predicts slightly more total organic acid production with TMI chemistry than without TMI chemistry during nighttime, but much less organic acid production during daytime with TMI chemistry compared to without TMI chemistry. In contrast, the CLEPS and Ervens models show 10%–20% higher organic acid mixing ratios with TMI chemistry compared to without TMI chemistry. These varying responses, especially in the amount of organic acid formation, to the addition of TMI chemistry suggest the representation of the TMI chemistry is important and points to the need for future evaluation.

4.5. Sensitivity to Variable pH (Simulation 5)

The simulations in Section 4.2 were repeated, prescribing the LWC to a set value (0.78 g kg^{-1}), but allowing the pH to be calculated by each model's method. Three of the models predict H^+ explicitly as part of the solution of the set of chemistry ODEs (Table 4). The Barth and Ervens models diagnose the H^+ concentration based on the electroneutrality equation for cations and anions. This set of simulations exposes differences among models in how they predict pH and its effect on organic acid production.

There are substantial differences in predicted pH among the models (Figure 13e), with values ranging from 4.0 to 4.8. The CAPRAM and Barth models predict similar pH values that initially are 4.3 and decrease to about 4.0. Differences between these models are a result of the Barth model having a reduced number of cations and anions in its electroneutrality equation. The CLEPS and GAMMA models predict similar pH during nighttime with a value of ~4.4, but during daytime the pH in the GAMMA model decreases as more organic acids are produced while the pH in the CLEPS model increases slightly as organic acid production decreases. The Ervens model predict higher values of pH during most of the simulation compared to the other models, which is likely due to different equilibrium coefficients. Sulfate and nitrate are the dominant anions throughout the simulation, although sulfate's contribution becomes smaller after sunrise because of the formation of HNO_3 and organic acids. The predicted mixing ratios and concentrations of total HO_2, total O_3, aqueous OH, and sum of total organic acids (Figure 13) change only a small amount between Simulation 2 (where pH = 4.5) and Simulation 5 (predicted pH), as the predicted pH is within a couple tenths of the prescribed pH.

The predicted pH of 4–4.5 is lower than what was measured (pH = 5.27 at 1800 LT, pH = 5.0 at 0600 LT) by ALSC. The higher measured pH is likely a result of the higher NH_4^+ measured in the drops than modeled, but could also partly be due to other cations, for example, calcium, magnesium, and potassium, contributing to the cloud pH (Christopher Lawrence, personal communication). Calcium and other trace metals were not included in the pH calculation for this sensitivity simulation, but likely exist as an external mixture to most cloud droplets prior to bulk cloud water collection (Pye et al., 2020). Assuming that all of the Ca^{2+} and Mg^{2+} measured by ALSC (8.1 and 3.9 μM, respectively) was externally mixed in a minor subset of the droplet population, the pH of the majority of cloud droplets prior to bulk collection is estimated to have been 4.5. Further, the models did not include dissolution of ammonia (NH_3) as part of the cloud drop composition. To test how much NH_3 is needed to reach higher pH values, the Barth model was used for several sensitivity studies with different gas-phase NH_3 mixing ratios. Increasing NH_3 to over 1 ppbv is needed (Figure 14) to balance the anions dissolved and formed in the cloud drops. Zhou et al. (2019) find NH_3 mixing ratios of ~1 ppbv at WFM, confirming the need for including NH_3 (g) in the pH calculation. Additional cations may also be needed to further increase pH. Further, the initial aerosol concentrations of sulfate, nitrate, and ammonium taken from the WRF-Chem simulation were somewhat different than what was measured by ALSC

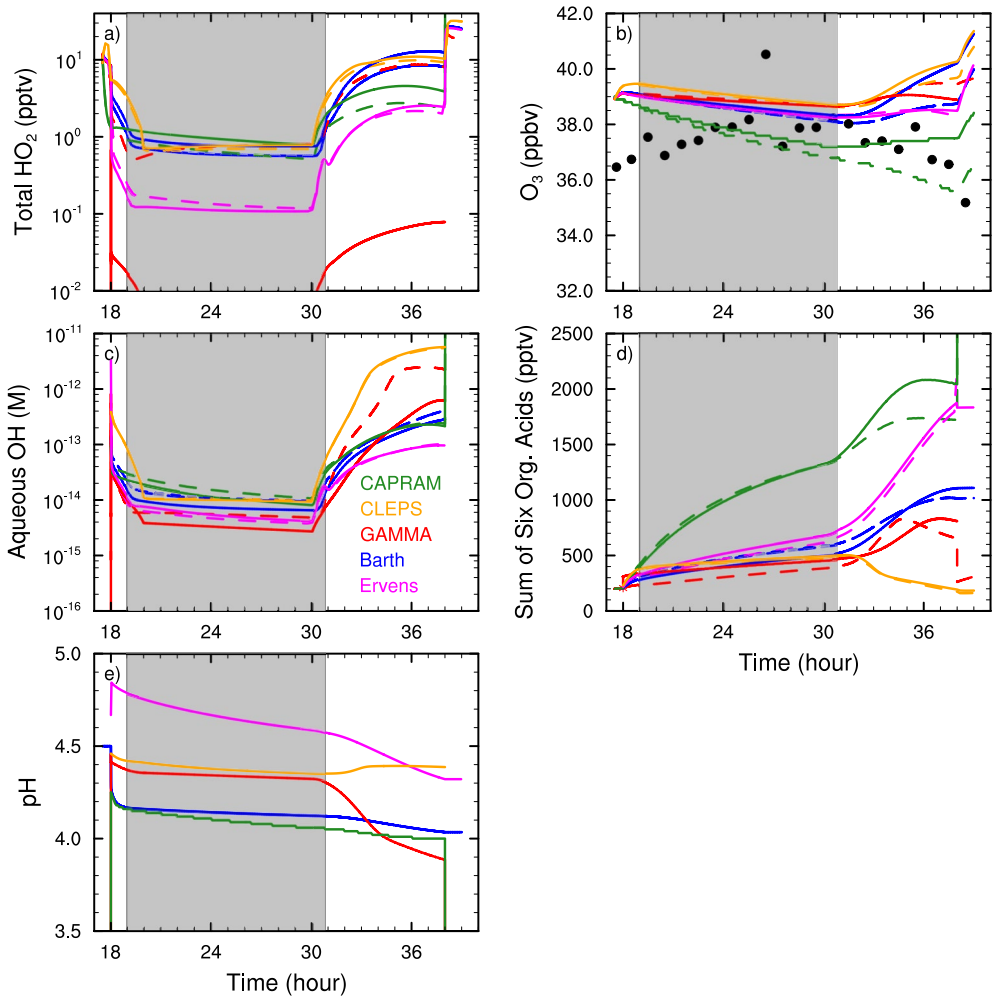

Figure 13. Time series from the cloud simulation with prescribed LWC and predicted pH (solid lines) and prescribed pH = 4.5 (dashed lines) of (a) total (gas + aqueous phases) HO_2 (pptv), (b) total O_3 (ppbv), (c) aqueous OH (M), (d) total of all organic acids (pptv), and (e) pH of the cloud water. Results are colored by different models, where green lines are CAPRAM, gold lines are CLEPS, red lines are GAMMA, blue lines are Barth, and magenta lines are Ervens models. The gray shaded region denotes nighttime. The black dots in the O_3 panel are hourly average observations from the WFM Summit Observatory measured by ASRC.

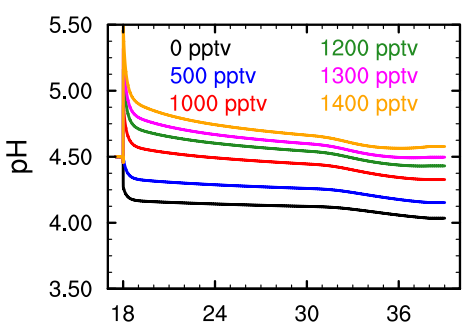

Figure 14. Time series of pH from the cloud simulation with prescribed LWC and predicted pH for different NH_3 mixing ratios. Results are from the Barth model.

(and reported after the simulations were performed). The ALSC measurements show higher NH_4^+ and slightly lower SO_4^{2-} concentrations. Using ALSC measured NH_4^+ and SO_4^{2-}, tests with the Barth model show that gas-phase NH_3 of ~1 ppbv is needed to obtain pH values of 5.0–5.3. These results emphasize the need to have gas-phase NH_3 measurements to characterize the composition and acidity of cloud water.

5. Conclusions

Five multiphase chemistry box models, with varying complexity of gas and aqueous chemistry, participated in a model intercomparison of cloud chemistry. The intercomparison focused on chemistry and mass transfer between the gas phase and cloud drops; thus, did not consider aerosol chemistry or physics. The chemical mechanisms were used in their standard configuration with only minor modifications of the code. Therefore, despite using the same model configuration for environmental

conditions and initial gas-phase and aerosol mixing ratios, differences in the gas and aqueous-phase chemical reactions and equilibria and in the description of phase transfer processes exist among the models. These differences in representation are seen in the results of the intercomparison.

Differences in gas-phase representation affect the gas-phase mixing ratios of important oxidants. Importantly, the OH mixing ratio differed by up to a factor of 10 during daytime among models for a simulation in which only gas-phase chemistry was represented. The predicted aldehyde and organic acid mixing ratios, because of different OH mixing ratios, displayed a 50%–500% spread among the models.

Differences in gas-aqueous chemistry simulations could often be attributed to different Henry's law and, to a smaller degree, different aqueous dissociation constants used by the five models. Uncertainties in Henry's law constants (e.g., acetyl peroxy radical H_{eff} is an estimated value that can affect acetic acid formation rates) and uncertainties in reaction rate constants can explain much of the differences between the five models. These equilibrium and rate constant differences suggest that these chemical data be reviewed by the community to provide recommended values. There are also differences in the mechanisms themselves that cause differences between model predictions. For example, the CAPRAM and Ervens models include different reaction pathways of acetyl peroxy radical which will produce acetic acid while the other three models do not include these reactions. Determining which of the different reaction pathways is the better representation of aqueous chemistry should be addressed with laboratory studies that provide a controlled environment. Cloud chambers could also provide controlled environmental and input chemical concentrations for investigating aspects of the integrated reaction system (e.g., aqueous SOA formation from IEPOX in the cloud drops). The discrepancies in the aqueous-phase chemistry mechanisms leading to differences in predicted oxidant and organic concentrations should motivate systematic evaluation of aqueous chemical reactions, such as the International Union on Pure and Applied Chemistry (IUPAC) task group on atmospheric chemical kinetic data evaluation. Efforts should also be made for creating reduced aqueous-phase chemical mechanisms that can be used by three-dimensional chemistry transport models.

Sensitivity simulations were conducted for (a) a different prescribed pH, and (b) inclusion of transition metal ion chemistry. Using a higher prescribed pH compared to the control simulation, produced different responses from the five models, especially for organic acid production. While the CAPRAM model has substantially less (35%) organic acid production because of less HCOOH production or more destruction, the other four models showed ±5% changes in total organic acid mixing ratios. The inclusion of TMI chemistry did impact model predictions of organic acid formation because HO_2 mixing ratios were reduced with TMI chemistry. This effect could be even more important than reported here because the TMI concentrations used in this study are rather low (<0.1 μM). Thus, TMI chemistry can potentially affect in-cloud production of secondary organic aerosol mass, suggesting this chemistry be included in chemistry transport models and recognizing there are still large uncertainties and gaps in the mechanisms related to TMI chemistry.

A simulation where the pH of the cloud water was predicted along with the gas and aqueous chemistry was also performed. As expected, when aqueous oxidation proceeds to form sulfuric and organic acids, the pH predicted by each of the models decreased during the cloud event by about 0.2 pH units. However, predicted pH among the models varied by up to 0.4 pH units. This result is not surprising as each model uses different equilibrium constants. It is important to remember that the pH value measured in bulk cloud water samples and simulated by bulk models with monodisperse droplet populations (as prescribed here) does not represent the pH in individual cloud droplets of different sizes originating from different CCN composition.

The intercomparison case study was based on a cloud event that occurred at the summit of Whiteface Mountain, New York, where some gas-phase trace gases, liquid water content, and some aqueous-phase species were measured. Model results were compared to observations for a few key species, for example, ozone and SO_2 in the gas phase, and sulfate, nitrate, ammonium, and total organic carbon in the aqueous phase. Good agreement was found between model predictions and ozone, but model predicted SO_2 (g) was quickly depleted while observations showed a sustained level of SO_2 (g), indicating that the air at Whiteface Mountain was replenished with new air parcels during the cloud event. Future model-observation comparisons need to account for air parcel trajectories and their history. Comparisons of model predicted sulfate and nitrate with observations were fairly good (within 20%), but the ammonium concentration used in the box models (taken from a WRF-Chem simulation) was 5–6 times less than that measured, suggesting that

NH_3 emissions used by the WRF-Chem model were low. Predicted organic carbon in the aqueous phase was also much lower than measured by 4 times, likely due to the low concentration initialized by WRF-Chem, which did not represent aerosol chemical reactions in its simulation, or to incomplete chemical mechanisms or less understood partitioning (e.g., van Pinxteren et al., 2005). Thus, future model-observation comparisons also need to either provide a wide suite of trace gas and aerosol composition measurements for box model intercomparisons, or, when using 3-d models to aid the initialization, need to have a robust representation of gas, aerosol, and cloud chemistry.

To understand the impact of cloud chemistry on organic aerosol mixing ratios, it is important to have detailed chemical mechanisms that are continuously developed to include recent kinetic and mechanistic advances. However, 3-d models need to employ simplified mechanisms to reduce computational costs (e.g., Deguillaume et al., 2009). The comparison among models shows that the simpler Barth and Ervens mechanisms reasonably represent aqueous OH concentrations compared to the highly complex CAPRAM model, however the simple mechanisms tended to produce lower organic acid concentrations in the aqueous phase compared to CAPRAM, mainly due to less acetic acid production. The spread in these model results suggests that further work is needed to create simplified representations of organic aqueous-phase chemistry, much like there is available for the gas-phase organic chemistry mechanisms.

The results presented here also suggest further model-observation comparisons must be done to evaluate our ability to represent and test our understanding of aqueous-phase processing of organic and inorganic cloud water constituents. Intensive observing periods during a variety of environmental conditions and with frequent (hourly or less) measurements in both the cloud inflow region and within cloud (preferably with both cloud water and interstitial air sampled) can provide such data. Other environments that are especially important to investigate include polluted regions with different mixes of VOCs and NO_x (e.g., East Asia with high VOCs and NO_x, South Asia, and North America with moderate VOCs and NO_x), and regions influenced by biomass burning, as well as clean marine and tropical conditions.

Data Availability Statement

Model output and observations presented in the study can be found at the Coordinated Cloud Chemistry web site, specifically https://www2.acom.ucar.edu/cloud-chemistry/box-model-intercomparison.

Acknowledgments
This cloud chemistry model intercomparison study is an outcome of the Whiteface Mountain Cloud Chemistry Workshop that occurred September 16–17, 2016 supported by NSF/AGS-1638579. NCAR is supported by the National Science Foundation. B. Ervens has been supported by the French National Research Agency (ANR) (grant no. ANR-17-MPGA0013). Support of part of the described TROPOS work by the DFG project ACoMa (grant number TI 925/1-1) is gratefully acknowledged. The authors thank John Orlando and Alma Hodzic for their comments on the paper. The authors thank the Adirondack Lake Survey, Rodney Weber, and Pierre Herckes for sharing their observational data. WFM trace gas and meteorological measurements were supported by the New York State Energy Research and Development Authority (NYSERDA) Contract 48971. Cloud water measurements during the time period discussed in this paper were supported by NYSERDA under the Adirondack Long Term Monitoring project.

References

Altieri, K. E., Carlton, A. G., Lim, H.-J., Turpin, B. J., & Seitzinger, S. P. (2006). Evidence for oligomer formation in clouds: Reactions of isoprene oxidation products. *Environmental Science & Technology*, *40*, 4956–4960. https://doi.org/10.1021/es052170n

Andreae, M. O., Talbot, R. W., Andreae, T. W., & Harriss, R. C. (1988). Formic and acetic acid over the central Amazon region, Brazil: 1. Dry season. *Journal of Geophysical Research: Atmospheres*, *93*(D2), 1616–1624. https://doi.org/10.1029/JD093iD02p01616

Arakaki, T., Anastasio, C., Kuroki, Y., Nakajima, H., Okada, K., Kotani, Y., et al. (2013). A general scavenging rate constant for reaction of hydroxyl radical with organic carbon in atmospheric waters. *Environmental Science & Technology*, *47*(15), 8196–8203. https://doi.org/10.1021/es401927b

Audiffren, N., Renard, M., Buisson, E., & Chaumerliac, N. (1998). Deviations from the Henry's law equilibrium during cloud events: A numerical approach of the mass transfer between phases and its specific numerical effects. *Atmospheric Research*, *49*(2), 139–161. https://doi.org/10.1016/S0169-8095(98)00072-6

Baray, J.-L., Deguillaume, L., Colomb, A., Sellegri, K., Freney, E., Rose, C., et al. (2020). Cézeaux-Aulnat-Opme-Puy De Dôme: A multi-site for the long-term survey of the tropospheric composition and climate change. *Atmospheric Measurement Techniques*, *13*, 3413–3445. https://doi.org/10.5194/amt-13-3413-2020

Barth, M. C., Sillman, S., Hudman, R., Jacobson, M. Z., Kim, C.-H., Monod, A., & Liang, J. (2003). Summary of the cloud chemistry modeling intercomparison: Photochemical box model simulation. *Journal of Geophysical Research: Atmospheres*, *108*, 4214. https://doi.org/10.1029/2002jd002673

Barth, M. C., Stuart, A. L., & Skamarock, W. C. (2001). Numerical simulations of the July 10 Stratospheric-Tropospheric Experiment: Radiation, aerosols and ozone/deep convection storm: Redistribution of soluble tracers. *Journal of Geophysical Research: Atmospheres*, *106*(12), 381–12400. https://doi.org/10.1029/2001JD900139

Bianco, A., Deguillaume, L., Vaïtilingom, M., Nicol, E., Baray, J.-L., Chaumerliac, N., & Bridoux, M. (2018). Molecular characterization of cloud water samples collected at the Puy de Dôme (France) by Fourier transform ion cyclotron resonance mass spectrometry. *Environmental Science & Technology*, *52*(18), 10275–10285. https://doi.org/10.1021/acs.est.8b01964

Bianco, A., Passananti, M., Perroux, H., Voyard, G., Mouchel-Vallon, C., Chaumerliac, N, et al. (2015). A better understanding of hydroxyl radical photochemical sources in cloud waters collected at the puy de Dôme station—Experimental versus modelled formation rates. *Atmospheric Chemistry and Physics*, *15*, 9191–9202. https://doi.org/10.5194/acp-15-9191-2015

Blando, J. D., & Turpin, B. J. (2000). Secondary organic aerosol formation in cloud and fog droplets: A literature evaluation of plausibility. *Atmospheric Environment*, *34*, 1623–1632. https://doi.org/10.1016/S1352-2310(99)00392-1

Boone, E. J., Laskin, A., Laskin, J., Wirth, C., Shepson, P. B., Stirm, B. H., & Pratt, K. A. (2015). Aqueous processing of atmospheric organic particles in cloud water collected via aircraft sampling. *Environmental Science & Technology*, *49*(14), 8523–8530. https://doi.org/10.1021/acs.est.5b01639

Boris, A. J., Lee, T., Park, T., Choi, J., Seo, S. J., & Collett, J. L., Jr. (2016). Fog composition at Baengnyeong Island in the eastern Yellow Sea: Detecting markers of aqueous atmospheric oxidations. *Atmospheric Chemistry and Physics*, *16*, 437–453. https://doi.org/10.5194/acp-16-437-2016

Bräuer, P. (2015). *Extension and application of a tropospheric aqueous phase chemical mechanism (CAPRAM) for aerosol and cloud models (Doctoral dissertation)*. University of Leipzig. Retrieved from https://ul.qucosa.de/landing-page/?tx_dlf[id]=https%3A//ul.qucosa.de/api/qucosa%253A13675/mets

Bräuer, P., Mouchel-Vallon, C., Tilgner, A., Mutzel, A., Böge, O., Rodigast, M, et al. (2019). Development of a protocol for the auto-generation of explicit aqueous-phase oxidation schemes of organic compounds. *Atmospheric Chemistry and Physics*, *19*, 9209–9239. https://doi.org/10.5194/acp-19-9209-2019

Carlton, A. M., Barth, M. C., & Lance, S. M. (2017). Designing mountaintop cloud experiments. *Eos*, *98*. https://doi.org/10.1029/2017EO072373

Chameides, W. L. (1984). The photochemistry of a remote marine stratiform cloud. *Journal of Geophysical Research*, *89*, 4739–4755. https://doi.org/10.1029/jd089id03p04739

Chatfield, R. B., & Crutzen, P. J. (1984). Sulfur dioxide in remote oceanic air: Cloud transport of reactive precursors. *Journal of Geophysical Research*, *89*, 7111–7132. https://doi.org/10.1029/JD089iD05p07111

Chen, J., Griffin, R., Grini, A., & Tulet, P. (2007). Modeling secondary organic aerosol formation through cloud processing of organic compounds. *Atmospheric Chemistry and Physics*, *7*(20), 5343–5355. https://doi.org/10.5194/acp-7-5343-2007

Ching, J. K. S., Shipley, S. T., & Browell, E. V. (1988). Evidence for cloud venting of mixed layer ozone and aerosols. *Atmospheric Environment*, *22*, 225–242. https://doi.org/10.1016/0004-6981(88)90030-3

Deguillaume, L., Charbouillot, T., Joly, M., Vaïtilingom, M., Parazols, M., Marinoni, A, et al. (2014). Classification of clouds sampled at the Puy de Dôme (France) based on 10 yr of monitoring of their physicochemical properties. *Atmospheric Chemistry and Physics*, *14*, 1485–1506. https://doi.org/10.5194/acp-14-1485-2014

Deguillaume, L., Leriche, M., Desboeufs, K., Mailhot, G., George, C., & Chaumerliac, N. (2005). Transition metals in atmospheric liquid phases: Sources, reactivity, and sensitive parameters. *Chemical Reviews*, *105*, 3388–3431. https://doi.org/10.1021/cr040649c

Deguillaume, L., Leriche, M., Monod, A., & Chaumerliac, N. (2004). The role of transition metal ions on HOx radicals in clouds: A numerical evaluation of its impact on multiphase chemistry. *Atmospheric Chemistry and Physics*, *4*, 95–110. https://doi.org/10.5194/acp-4-95-2004

Deguillaume, L., Tilgner, A., Schrödner, R., Wolke, R., Chaumerliac, N., Herrmann, H. (2009). Towards an operational aqueous phase chemistry mechanism for regional chemistry-transport models: CAPRAM-RED and its application to the COSMO-MUSCAT model. *Journal of Atmospheric Chemistry*, *64*, 1–35. https://doi.org/10.1007/s10874-010-9168-8

Dickerson, R. R., Huffman, G. J., Luke, W. T., Nunnermacker, L. J., Pickering, K. E., Leslie, A. C. D., et al. (1987). Thunderstorms: An important mechanism in the transport of air pollutants. *Science*, *235*, 460–465. https://doi.org/10.1126/science.235.4787.460

Dominutti, P. A., Renard, P., Vaïtilingom, M., Bianco, A., Baray, J.-L., Borbon, A., et al. (2021). Insights into tropical cloud chemistry at Reunion Island (Indian Ocean): Results from the BIO-MAÏDO campaign, *Atmospheric Chemistry and Physics Discussions*, https://doi.org/10.5194/acp-2021-518

Doussin, J.-F., & Monod, A. (2013). Structure–activity relationship for the estimation of OH-oxidation rate constants of carbonyl compounds in the aqueous phase. *Atmospheric Chemistry and Physics*, *13*, 11625–11641. https://doi.org/10.5194/acp-13-11625-2013

Emmons, L. K., Walters, S., Hess, P. G., Lamarque, J.-F., Pfister, G. G., Fillmore, D., et al. (2010). Description and evaluation of the Model for Ozone and Related chemical Tracers, version 4 (MOZART-4). *Geoscientific Model Development*, *3*, 43–67. https://doi.org/10.5194/gmd-3-43-2010

Ervens, B. (2015). Modeling the processing of aerosol and trace gases in clouds and fogs. *Chemical Reviews*, *115*, 4157–4198. https://doi.org/10.1021/cr5005887

Ervens, B., Carlton, A. G., Turpin, B. J., Altieri, K. E., Kreidenweis, S. M., & Feingold, G. (2008). Secondary organic aerosol yields from cloud processing of isoprene oxidation products. *Geophysical Research Letters*, *35*, L02816. https://doi.org/10.1029/2007GL031828

Ervens, B., George, C., Williams, J. E., Buxton, G. V., Salmon, G. A., Bydder, M., et al. (2003). CAPRAM2.4 (MODAC mechanism): An extended and condensed tropospheric aqueous phase mechanism and its application. *Journal of Geophysical Research: Atmospheres*, *108*, 4426. https://doi.org/10.1029/2002JD002202

Ervens, B., Herckes, P., Feingold, G., Lee, T., Collett, J. L., Jr., & Kreidenweis, S. M. (2003). On the drop-size dependence of organic acid and formaldehyde concentrations in fog. *Journal of Atmospheric Chemistry*, *46*, 239–269. https://doi.org/10.1023/A:1026393805907

Ervens, B., Sorooshian, A., Lim, Y. B., & Turpin, B. J. (2014). Key parameters controlling the formation of secondary organic aerosol in the aqueous phase (aqSOA). *Journal of Geophysical Research: Atmospheres*, *119*, 3997–4016. https://doi.org/10.1002/2013JD021021

Ervens, B., Turpin, B. J., & Weber, R. J. (2011). Secondary organic aerosol formation in cloud droplets and aqueous particles (aqSOA): A review of laboratory, field and model studies. *Atmospheric Chemistry and Physics*, *11*, 11069–11102. https://doi.org/10.5194/acp-11-11069-2011

Fahey, K. M., Carlton, A. G., Pye, H. O. T., Baek, J., Hutzell, W. T., Stanier, C. O., et al. (2017). A framework for expanding aqueous chemistry in the Community Multiscale Air Quality (CMAQ) model version 5.1. *Geoscientific Model Development*, *10*, 1587–1605. https://doi.org/10.5194/gmd-10-1587-2017

Falconer, R., & Falconer, P. (1980). Determination of cloud water acidity at a mountain observatory in the Adirondack Mountains of New York State. *Journal of Geophysical Research*, *85*, 7465–7470. https://doi.org/10.1029/JC085iC12p07465

Faust, B. C., & Zepp, R. G. (1993). Photochemistry of aqueous iron(III)-polycarboxylate complexes: Roles in the chemistry of atmospheric and surface waters. *Environmental Science & Technology*, *27*(12), 2517–2522. https://doi.org/10.1021/es00048a032

Feingold, G., Kreidenweis, S. M., & Zhang, Y. (1998). Stratocumulus processing of gases and cloud condensation nuclei: 1. Trajectory ensemble model. *Journal of Geophysical Research: Atmospheres*, *103*(D16), 19527–19542. https://doi.org/10.1029/98JD01750

Gong, W., Stroud, C., & Zhang, L. (2011). Cloud processing of gases and aerosols in air quality modeling. *Atmosphere*, *2*, 567–616. https://doi.org/10.3390/atmos2040567

Guo, J., Wang, Y., Shen, X., Wang, Z., Lee, T., Wang, X., et al. (2012). Characterization of cloud water chemistry at Mount Tai, China: Seasonal variation, anthropogenic impact, and cloud processing. *Atmospheric Environment*, *60*, 467–476. https://doi.org/10.1016/j.atmosenv.2012.07.016

Hegg, D. A., & Hobbs, P. V. (1986). Sulfate and nitrate chemistry in cumuliform clouds. *Atmospheric Environment*, *20*, 901–909. https://doi.org/10.1016/0004-6981(86)90274-X

Herckes, P., Valsaraj, K. T., & Collett, J. L. (2013). A review of observations of organic matter in fogs and clouds: Origin, processing and fate. *Atmospheric Research*, *132–133*, 434–449. https://doi.org/10.1016/j.atmosres.2013.06.005

Herrmann, H., Tilgner, A., Barzaghi, P., Majdik, Z., Gligorovski, S., Poulain, L., & Monod, A. (2005). Towards a more detailed description of tropospheric aqueous phase organic chemistry: CAPRAM 3.0. *Atmospheric Environment*, *39*(23–24), 4351–4363. https://doi.org/10.1016/j.atmosenv.2005.02.016

Herrmann, H., Wolke, R., Müller, K., Brüggemann, E., Gnauk, T., Barzaghi, P, et al. (2005). FEBUKO and MODMEP: Field measurements and modelling of aerosol and cloud multiphase processes. *Atmospheric Environment*, *39*, 4169–4183. https://doi.org/10.1016/j.atmosenv.2005.02.004

Hindmarsh, A. C. (1983). *Scientific computing chapter ODEPACK: A systematized collection of ode solvers* (pp. 55–74).

Horowitz, L. W., Walters, S., Mauzerall, D. L., Emmons, L. K., Rasch, P. J., Granier, C., et al. (2003). A global simulation of tropospheric ozone and related tracers: Description and evaluation of MOZART, version 2. *Journal of Geophysical Research: Atmospheres*, *108*(D24), 4784. https://doi.org/10.1029/2002JD002853

Jacob, D. J. (1986). Chemistry of OH in remote clouds and its role in the production of formic acid and peroxymonosulfate. *Journal of Geophysical Research: Atmospheres*, *91*(D9), 9807–9826. https://doi.org/10.1029/JD091iD09p09807

Jenkin, M. E., Young, J. C., & Rickard, A. R. (2015). The MCMv3.3.1 degradation scheme for isoprene. *Atmospheric Chemistry and Physics*, *15*, 11433–11459. https://doi.org/10.5194/acp-15-11433-2015

Kim, S.-W., Barth, M. C., & Trainer, M. (2012). Influence of fair-weather clouds on isoprene chemistry. *Journal of Geophysical Research: Atmospheres*, *117*, D10302. https://doi.org/10.1029/2011JD017099

Lamarque, J.-F., Dentener, F., McConnell, J., Ro, C.-U., Shaw, M., Vet, R., et al. (2013). Multi-model mean nitrogen and sulfur deposition from the Atmospheric Chemistry and Climate Model Intercomparison Project (ACCMIP): Evaluation of historical and projected future changes. *Atmospheric Chemistry and Physics*, *13*, 7997–8018. https://doi.org/10.5194/acp-13-7997-2013

Lance, S., Zhang, J., Schwab, J. J., Casson, P., Brandt, R. E., Fitzjarrald, D. R., et al. (2020). Overview of the CPOC Pilot Study at Whiteface Mountain, NY: Cloud Processing of Organics within Clouds (CPOC). *Bulletin of the American Meteorological Society*, *101*(10), E1820–E1841. https://doi.org/10.1175/BAMS-D-19-0022.1

Lance, S. M., Barth, M. C., & Carlton, A. M. (2017). Multiphase chemistry: Experimental design for coordinated measurement and modeling of cloud processing at a mountaintop. *Bulletin of the American Meteorological Society*, *98*, ES163–ES167. https://doi.org/10.1175/bams-d-17-0015.1

Leriche, M., Curier, R. L., Deguillaume, L., Caro, D., Sellegri, K., & Chaumerliac, N. (2007). Numerical quantification of sources and phase partitioning of chemical species in cloud: Application to wintertime anthropogenic air masses at the Puy de Dôme station. *Journal of Atmospheric Chemistry*, *57*, 281–297. https://doi.org/10.1007/s10874-007-9073-y

Leriche, M., Deguillaume, L., & Chaumerliac, N. (2003). Modeling study of strong acids formation and partitioning in a polluted cloud during wintertime. *Journal of Geophysical Research: Atmospheres*, *108*, 1984–2012. https://doi.org/10.1029/2002JD002950

Leriche, M., Pinty, J.-P., Mari, C., & Gazen, D. (2013). A cloud chemistry module for the 3-D cloud-resolving mesoscale model Meso-NH with application to idealized cases. *Geoscientific Model Development*, *6*, 1275–1298. https://doi.org/10.5194/gmd-6-1275-2013

Leriche, M., Voisin, D., Chaumerliac, N., Monod, A., & Aumont, B. (2000). A model for tropospheric multiphase chemistry: Application to one cloudy event during the CIME experiment. *Atmospheric Environment*, *34*, 5015–5036. https://doi.org/10.1016/S1352-2310(00)00329-0

Li, S.-M., Macdonald, A. M., Leithead, A., Leaitch, W. R., Gong, W., Anlauf, K. G., et al. (2008). Investigation of carbonyls in cloudwater during ICARTT. *Journal of Geophysical Research: Atmospheres*, *113*, D17206. https://doi.org/10.1029/2007JD009364

Li, Y., Barth, M. C., Patton, E. G., & Steiner, A. L. (2017). Impact of in-cloud aqueous processes on the chemistry and transport of biogenic volatile organic compounds. *Journal of Geophysical Research: Atmospheres*, *122*, 11–131. https://doi.org/10.1002/2017JD026688

Lim, Y. B., Tan, Y., Perri, M. J., Seitzinger, S. P., & Turpin, B. J. (2010). Aqueous chemistry and its role in secondary organic aerosol (SOA) formation. *Atmospheric Chemistry and Physics*, *10*, 10521–10539. https://doi.org/10.5194/acp-10-10521-2010

Lin, G., Sillman, S., Penner, J. E., & Ito, A. (2014). Global modeling of SOA: The use of different mechanisms for aqueous-phase formation. *Atmospheric Chemistry and Physics*, *14*, 5451–5475. https://doi.org/10.5194/acp-14-5451-2014

Long, Y., Charbouillot, T., Brigante, M., Mailhot, G., Delort, A.-M., Chaumerliac, N., & Deguillaume, L. (2013). Evaluation of modeled cloud chemistry mechanism against laboratory irradiation experiments: The HxOy/iron/carboxylic acid chemical system. *Atmospheric Environment*, *77*, 686–695. https://doi.org/10.1016/j.atmosenv.2013.05.037

McNeill, V. F. (2015). Aqueous organic chemistry in the atmosphere: Sources and chemical processing of organic aerosols. *Environmental Science & Technology*, *49*, 1237–1244. https://doi.org/10.1021/es5043707

McNeill, V. F., Woo, J. L., Kim, D. D., Schwier, A. N., Wannell, N. J., Sumner, A. J., & Barakat, J. M. (2012). Aqueous-phase secondary organic aerosol and organosulfate formation in atmospheric aerosols: A modeling study. *Environmental Science & Technology*, *46*, 8075–8081. https://doi.org/10.1021/es3002986

Minakata, D., Li, K., Westerhoff, P., & Crittenden, J. (2009). Development of a group contribution method to predict aqueous phase hydroxyl radical (HO) reaction rate constants. *Environmental Science & Technology*, *43*, 6220–6227. https://doi.org/10.1021/es900956c

Möhnen, V., & Kadlecek, J. (1989). Cloud chemistry research at Whiteface Mountain. *Tellus*, 79–91. https://doi.org/10.3402/tellusb.v41i1.15052

Monod, A., & Doussin, J. F. (2008). Structure-activity relationship for the estimation of OH-oxidation rate constants of aliphatic organic compounds in the aqueous phase: Alkanes, alcohols, organic acids and bases. *Atmospheric Environment*, *42*, 7611–7622. https://doi.org/10.1016/j.atmosenv.2008.06.005

Mouchel-Vallon, C., Deguillaume, L., Monod, A., Perroux, H., Rose, C., Ghigo, G., et al. (2017). CLEPS 1.0: A new protocol for cloud aqueous phase oxidation of VOC mechanisms. *Geoscientific Model Development*, *10*, 1339–1362. https://doi.org/10.5194/gmd-10-1339-2017

Munger, J. W., Collett, J., Jr., Daube, B. C., Jr., & Hoffmann, M. R. (1989). Carboxylic acids and carbonyl compounds in southern California clouds and fogs. *Tellus B: Chemical and Physical Meteorology*, *41*, 230–242. https://doi.org/10.3402/tellusb.v41i3.15074

Paulson, S. E., Gallimore, P. J., Kuang, X. M., Chen, J. R., Kalberer, M., & Gonzalez, D. H. (2019). A light-driven burst of hydroxyl radicals dominates oxidation chemistry in newly activated cloud droplets. *Science Advances*, *5*, EAAV7689. https://doi.org/10.1126/sciadv.aav7689

Pye, H. O. T., Nenes, A., Alexander, B., Ault, A. P., Barth, M. C., Clegg, S. L., et al. (2020). The acidity of atmospheric particles and clouds. *Atmospheric Chemistry and Physics*, *20*, 4809–4888. https://doi.org/10.5194/acp-20-4809-2020

Raventos-Duran, T., Camredon, M., Valorso, R., Mouchel-Vallon, C., & Aumont, B. (2010). Structure-activity relationships to estimate the effective Henry's law constants of organics of atmospheric interest. *Atmospheric Chemistry and Physics*, *10*, 7643–7654. https://doi.org/10.5194/acp-10-7643-2010

Renard, P., Bianco, A., Baray, J.-L., Bridoux, M., Delort, A.-M., & Deguillaume, L. (2020). Classification of clouds sampled at the Puy de Dôme station (France) based on chemical measurements and air mass history matrices. *Atmosphere*, *11*, 732. https://doi.org/10.3390/atmos11070732

Rosanka, S., Sander, R., Wahner, A., & Taraborrelli, D. (2020). Oxidation of low-molecular weight organic compounds in cloud droplets: Development of the JAMOC chemical mechanism in CAABA/MECCA (version 4.5.0gmdd). *Geoscientific Model Development Discussions*. https://doi.org/10.5194/gmd-2020-337

Rose, C., Chaumerliac, N., Deguillaume, L., Perroux, H., Mouchel-Vallon, C., Leriche, M., et al. (2018). Modeling the partitioning of organic chemical species in cloud phases with CLEPS (1.1). *Atmospheric Chemistry and Physics*, *18*, 2225–2242. https://doi.org/10.5194/acp-18-2225-2018

Sandu, A., & Sander, R. (2006). Technical note: Simulating chemical systems in Fortran90 and Matlab with the Kinetic PreProcessor KPP-2.1. *Atmospheric Chemistry and Physics*, *6*, 187–195. https://doi.org/10.5194/acp-6-187-2006

Saunders, S. M., Pascoe, S., Johnson, A. P., Pilling, M. J., & Jenkin, M. E. (2003). Development and preliminary test results of an expert system for the automatic generation of tropospheric VOC degradation mechanisms. *Atmospheric Environment*, *37*, 1723–1735. https://doi.org/10.1016/S1352-2310(03)00072-4

Schneider, J., Mertes, S., van Pinxteren, D., Herrmann, H., & Borrmann, S. (2017). Uptake of nitric acid, ammonia, and organics in orographic clouds: Mass spectrometric analyses of droplet residual and interstitial aerosol particles. *Atmospheric Chemistry and Physics*, *17*, 1571–1593. https://doi.org/10.5194/acp-17-1571-2017

Schwab, J. J., Casson, P., Brandt, R., Husain, L., Dutkewicz, V., Wolfe, D., et al. (2016). Atmospheric chemistry measurements at Whiteface Mountain, NY: Cloud water chemistry, Precipitation chemistry, and particulate matter. *Aerosol and Air Quality Research*, *16*, 16841–16854. https://doi.org/10.4209/aaqr.2015.05.0344

Schwab, J. J., Wolfe, D., CassonBrandt, P. W. R. E., Demerjian, K. L., Husain, L., Dutkiewicz, V. A., et al. (2016). Atmospheric science research at Whiteface Mountain, NY: Site description and history. *Aerosol and Air Quality Research*, *16*, 16827–16840. https://doi.org/10.4209/aaqr.2015.05.0343

Schwartz, S. E. (1986). Mass transport considerations pertinent to aqueous phase reactions of gases in liquid water clouds. In W. Jaeschke (Ed.), *Chemistry of multiphase atmospheric systems. NATO ASI series* (Vol. *G6*, pp. 415–471). Springer. https://doi.org/10.1007/978-3-642-70627-1_16

Sehili, A. M., Wolke, R., Knoth, O., Simmel, M., Tilgner, A., & Herrmann, H. (2005). Comparison of different model approaches for the simulation of multiphase processes. *Atmospheric Environment*, *39*, 4403–4417. https://doi.org/10.1016/j.atmosenv.2005.02.039

Seinfeld, J. H., & Pandis, S. N. (2016). *Atmospheric chemistry and physics: From air pollution to climate change* (3rd ed., p. 1152). John Wiley & Sons.

Sellegri, K., Laj, P., Marinoni, A., Dupuy, R., Legrand, M., & Preunken, S. (2003). Contribution of gaseous and particulate species to droplet solute composition at the Puy de Dôme, France. *Atmospheric Chemistry and Physics*, *3*, 1509–1522. https://doi.org/10.5194/acp-3-1509-2003

Siefert, R. L., JohansenHoffmann, A. M. M. R., Pehkonen, S. O., & Pehkonen, S. O. (1998). Measurements of Trace Metal (Fe, Cu, Mn, Cr) Oxidation States in Fog and Stratus Clouds. *Journal Air and Waste Management Association*, *48*, 128–143. https://doi.org/10.1080/10473289.1998.10463659

Siefert, R. L., Webb, S. M., & Hoffmann, M. R. (1996). Determination of photochemically available iron in ambient aerosols. *Journal of Geophysical Research: Atmospheres*, *101*, 14441–14449. https://doi.org/10.1029/96JD00857

Simmel, M., Diehl, K., & Wurzler, S. (2005). Numerical simulation of the microphysics of an orographic cloud: Comparison with measurements and sensitivity studies. *Atmospheric Environment*, *39*, 4365–4373. https://doi.org/10.1016/j.atmosenv.2005.02.017

Simmel, M., & Wurzler, S. (2006). Condensation and activation in sectional cloud microphysical models. *Atmospheric Research*, *80*, 218–236. https://doi.org/10.1016/j.atmosres.2005.08.002

Sorooshian, A., Varutbangkul, V., Brechtel, F. J., Ervens, B., Feingold, G., Bahreini, R., et al. (2006). Oxalic acid in clear and cloudy atmospheres: Analysis of data from International Consortium for Atmospheric Research on Transport and Transformation 2004. *Journal of Geophysical Research: Atmospheres*, *111*, D23S45. https://doi.org/10.1029/2005JD006880

Sorooshian, A., Wang, Z., Coggon, M. M., Jonsson, H. H., & Ervens, B. (2013). Observations of sharp oxalate reductions in stratocumulus clouds at variable altitudes: Organic acid and metal measurements during the 2011 E-PEACE Campaign. *Environmental Science & Technology*, *47*(14), 7747–7756. https://doi.org/10.1021/es4012383

Straub, D. J., Hutchings, J. W., & Herckes, P. (2012). Measurements of fog composition at a rural site. *Atmospheric Environment*, *47*, 195–205. https://doi.org/10.1016/j.atmosenv.2011.11.014

Sullivan, A. P., Weber, R. J., Clements, A. L., Turner, J. R., Bae, M. S., & Schauer, J. J. (2004). A method for on-line measurement of water-soluble organic carbon in ambient aerosol particles: Results from an urban site. *Geophysical Research Letters*, *31*, L13105. https://doi.org/10.1029/2004GL019681

Tilgner, A., Bräuer, P., Wolke, R., & Herrmann, H. (2013). Modelling multiphase chemistry in deliquescent aerosols and clouds using CAPRAM3.0i. *Journal of Atmospheric Chemistry*, *70*, 221–256. https://doi.org/10.1007/s10874-013-9267-4

Tilgner, A., & Herrmann, H. (2010). Radical-driven carbonyl-to-acid conversion and acid degradation in tropospheric aqueous systems studied by CAPRAM. *Atmospheric Environment*, *44*, 5415–5422. https://doi.org/10.1016/j.atmosenv.2010.07.050

Tilgner, A. & Herrmann, H. (2018). Tropospheric aqueous-phase OH oxidation chemistry: Current understanding, uptake of highly oxidized organics and its effects. In S. W. Hunt, A. Laskin, & S. A. Nizkorodov (Eds.), *Multiphase environmental chemistry in the atmosphere* (pp. 49–85). American Chemical Society. https://doi.org/10.1021/bk-2018-1299.ch004

Tilgner, A., Schaefer, T., Alexander, B., Barth, M., Collett, J. L., Fahey, K. M., et al. (2021). Acidity and the multiphase chemistry of atmospheric aqueous particles and clouds, *Atmospheric Chemistry and Physics Discussions*. https://doi.org/10.5194/acp-2021-58

Tsui, W. G., Woo, J. L., & McNeill, V. F. (2019). Impact of aerosol-cloud cycling on aqueous secondary organic aerosol formation. *Atmosphere*, *10*, 666–678. https://doi.org/10.3390/atmos10110666

van Pinxteren, D., Fomba, K. W., Mertes, S., Müller, K., Spindler, G., Schneider, J., et al. (2016). Cloud water composition during HCCT-2010: Scavenging efficiencies, solute concentrations, and droplet size dependence of inorganic ions and dissolved organic carbon. *Atmospheric Chemistry and Physics*, *16*, 3185–3205. https://doi.org/10.5194/acp-16-3185-2016

van Pinxteren, D., Plewka, A., Hofmann, D., Müller, K., Kramberger, H., Svrcina, B., et al. (2005). Schmücke hill cap cloud and valley stations aerosol characterisation during FEBUKO (II): Organic compounds. *Atmospheric Environment*, *39*, 4305–4320. https://doi.org/10.1016/j.atmosenv.2005.02.014

Voisin, D., Legrand, M., & Chaumerliac, N. (2000). Scavenging of acidic gases (HCOOH, CH_3COOH, HNO_3, HCl, and SO_2) and ammonia in mixed liquid-solid water clouds at the Puy de Dôme mountain (France). *Journal of Geophysical Research: Atmospheres*, *105*, 6817–6835. https://doi.org/10.1029/1999JD900983

Wang, M., Perroux, H., Fleuret, J., Bianco, A., Bouvier, L., Colomb, A., et al. (2020). Anthropogenic and biogenic hydrophobic VOCs detected in clouds at the Puy de Dôme station using Stir Bar Sorptive Extraction: Deviation from the Henry's law prediction. *Atmospheric Research*, *237*, 104844. https://doi.org/10.1016/j.atmosres.2020.104844

Weller, C., Tilgner, A., Brauer, P., & Herrmann, H. (2014). Modeling the impact of iron-carboxylate photochemistry on radical budget and carboxylate degradation in cloud droplets and particles. *Environmental Science & Technology*, *48*(10), 5652–5659. https://doi.org/10.1021/es4056643

Winiwarter, W., Fierlinger, H., Puxbaum, H., Facchini, M. C., Arends, B. G., Fuzzi, S., et al. (1994). Henry's law and the behavior of weak acids and bases in fog and cloud. *Journal of Atmospheric Chemistry*, *19*, 173–188. https://doi.org/10.1007/BF00696588

Wolke, R., & Knoth, O. (2002). Time-integration of multiphase chemistry in size-resolved cloud models. *Applied Numerical Mathematics*, *42*, 473–487. https://doi.org/10.1016/S0168-9274(01)00169-6

Wolke, R., Sehili, A. M., Simmel, M., Knoth, O., Tilgner, A., & Herrmann, H. (2005). SPACCIM: A parcel model with detailed microphysics and complex multiphase chemistry. *Atmospheric Environment*, *39*, 4375–4388. https://doi.org/10.1016/j.atmosenv.2005.02.038

Xue, J., Yuan, Z., Griffith, S. M., Yu, X., Lau, A. K. H., & Yu, J. Z. (2016). Sulfate formation enhanced by a cocktail of high NO_x, SO_2, Particulate matter, and droplet pH during haze-fog events in megacities in China: An observation-based modeling investigation. *Environmental Science & Technology*, *50*(14), 7325–7334. https://doi.org/10.1021/acs.est.6b00768

Zhou, C., Zhou, H., Holsen, T. M., Hopke, P. K., Edgerton, E. S., & Schwab, J. J. (2019). Ambient ammonia concentrations across New York State. *Journal of Geophysical Research: Atmospheres*, *124*, 8287–8302. https://doi.org/10.1029/2019JD030380

Zhu, Y., Tilgner, A., Hoffmann, E. H., Herrmann, H., Kawamura, K., Yang, L., et al. (2020). Multiphase MCM-CAPRAM modeling of the formation and processing of secondary aerosol constituents observed during the Mt. Tai summer campaign in 2014. *Atmospheric Chemistry and Physics*, *20*, 6725–6747. https://doi.org/10.5194/acp-20-6725-2020

References From the Supporting Information

Chen, F., & Dudhia, J. (2001). Coupling an advanced land surface–Hydrology model with the Penn State–NCAR MM5 Modeling System. Part I: Model implementation and sensitivity. *Monthly Weather Review*, *129*, 569–585. https://doi.org/10.1175/1520-0493(2001)129<0569:CAALSH>2.0.CO;2

Easter, R. C., Ghan, S. J., Zhang, Y., Saylor, R. D., Chapman, E. G., Laulainen, N. S., et al. (2004). MIRAGE: Model description and evaluation of aerosols and trace gases. *Journal of Geophysical Research: Atmospheres*, *109*, D20210. https://doi.org/10.1029/2004JD004571

Emmons, L. K., Walters, S., Hess, P. G., Lamarque, J.-F., Pfister, G. G., Fillmore, D., et al. (2010). Description and evaluation of the Model for Ozone and Related chemical Tracers, version 4 (MOZART-4). *Geoscientific Model Development*, *3*, 43–67. https://doi.org/10.5194/gmd-3-43-2010

Fast, J. D., Gustafson, W. I., Jr., Easter, R. C., Zaveri, R. A., Barnard, J. C., Chapman, E. G., et al. (2006). Evolution of ozone, particulates, and aerosol direct radiative forcing in the vicinity of Houston using a fully coupled meteorology-chemistry-aerosol model. *Journal of Geophysical Research: Atmospheres*, *111*, D21305. https://doi.org/10.1029/2005JD006721

Grell, G., Freitas, S. R., Stuefer, M., & Fast, J. (2011). Inclusion of biomass burning in WRF-Chem: Impact of wildfires on weather forecasts. *Atmospheric Chemistry and Physics*, *11*, 5289–5303. https://doi.org/10.5194/acp-11-5289-2011

Grell, G. A., & Freitas, S. R. (2014). A scale and aerosol aware stochastic convective parameterization for weather and air quality modeling. *Atmospheric Chemistry and Physics*, *14*(10), 5233–5250. https://doi.org/10.5194/acp-14-5233-2014

Grell, G. A., Peckham, S. E., Schmitz, R., McKeen, S. A., Frost, G., Skamarock, W. C., & Eder, B. (2005). Fully coupled "online" chemistry within the WRF model. *Atmospheric Environment*, *39*, 6957–6975. https://doi.org/10.1016/j.atmosenv.2005.04.027

Guenther, A., Karl, T., Harley, P., Wiedinmyer, C., Palmer, P. I., & Geron, C. (2006). Estimates of global terrestrial isoprene emissions using MEGAN (Model of Emissions of Gases and Aerosols from Nature). *Atmospheric Chemistry and Physics*, *6*, 3181–3210. https://doi.org/10.5194/acp-6-3181-2006

Hodzic, A., & Jimenez, J. (2011). Modeling anthropogenically controlled secondary organic aerosols in a megacity: A simplified framework for global and climate models. *Geoscientific Model Development*, *4*, 901–917. https://doi.org/10.5194/gmd-4-901-2011

Iacono, M. J., Delamere, J. S., Mlawer, E. J., Shephard, M. W., Clough, S. A., & Collins, W. D. (2008). Radiative forcing by long-lived greenhouse gases: Calculations with the AER radiative transfer models. *Journal of Geophysical Research: Atmospheres*, *113*. https://doi.org/10.1029/2008JD009944

Janjić, Z. I. (1994). The Step-Mountain Eta Coordinate Model: Further developments of the convection, viscous sublayer, and turbulence closure schemes. *Monthly Weather Review*, *122*, 927–945. https://doi.org/10.1175/1520-0493(1994)122<0927:TSMECM>2.0.CO;2

Knote, C., Hodzic, A., Jimenez, J. L., Volkamer, R., Orlando, J. J., Baidar, S., et al. (2014). Simulation of semi-explicit mechanisms of SOA formation from glyoxal in aerosol in a 3-D model. *Atmospheric Chemistry and Physics*, *14*, 6213–6239. https://doi.org/10.5194/acp-14-6213-2014

LeGrand, S. I., Polashenski, C. C., Letcher, T. W., Creighton, G. A., Peckham, S. E., & Cetola, J. D. (2019). The AFWA dust emission scheme for the GOCART aerosol model in WRF-Chem v3.8.1. *Geoscientific Model Development*, *12*, 131–166. https://doi.org/10.5194/gmd-12-131-2019

Morrison, H., Thompson, G., & Tatarskii, V. (2009). Impact of cloud microphysics on the development of trailing stratiform precipitation in a simulated squall line: Comparison of one- and two-moment schemes. *Monthly Weather Review*, *137*, 991–1007. https://doi.org/10.1175/2008MWR2556.1

Neu, J. L., & Prather, M. J. (2012). Toward a more physical representation of precipitation scavenging in global chemistry models: Cloud overlap and ice physics and their impact on tropospheric ozone. *Atmospheric Chemistry and Physics*, *12*(7), 3289–3310. https://doi.org/10.5194/acp-12-3289-2012

Price, C., & Rind, D. (1992). A simple lightning parameterization for calculating global lightning distributions. *Journal of Geophysical Research*, *97*, 9919–9933. https://doi.org/10.1029/92JD00719

Sandu, A., & Sander, R. (2006). Technical note: Simulating chemical systems in Fortran90 and Matlab with the Kinetic PreProcessor KPP-2.1. *Atmospheric Chemistry and Physics*, *6*, 187–195. https://doi.org/10.5194/acp-6-187-2006

Shrivastava, M., Fast, J., Easter, R., Gustafson, W. I., Jr., Zaveri, R. A., Jimenez, J. L., et al. (2011). Modeling organic aerosols in a megacity: Comparison of simple and complex representations of the volatility basis set approach. *Atmospheric Chemistry and Physics*, *11*, 6639–6662. https://doi.org/10.5194/acp-11-6639-2011

Skamarock, W. C., Klemp, J. B., Dudhia, J., Gill, D. O., Barker, D., Duda, M. G., et al. (2008). *A description of the advanced research WRF version 3 (No. NCAR/TN-475+STR)*. University Corporation for Atmospheric Research. https://doi.org/10.5065/D68S4MVH

Wang, H., Skamarock, W., & Feingold, G. (2009). Evaluation of scalar advection schemes in the advanced research WRF model using large-eddy simulations of aerosol-cloud interactions. *Monthly Weather Review*, *137*, 2547–2558. https://doi.org/10.1175/2009MWR2820.1

Wesely, M. (1989). Parameterization of surface resistances to gaseous dry deposition in regional-scale numerical models. *Atmospheric Environment*, *23*, 1293–1304. https://doi.org/10.1016/j.atmosenv.2007.10.058

WiedinmyerAkagi, C. S. K., Yokelson, R. J., Emmons, L. K., Al-Saadi, J. A., Orlando, J. J., & Soja, A. J. (2011). The Fire INventory from NCAR (FINN): A high resolution global model to estimate the emissions from open burning. *Geoscientific Model Development*, *4*, 625–641. https://doi.org/10.5194/gmd-4-625-2011

Wong, J., Barth, M. C., & Noone, D. (2013). Evaluating a lightning parameterization based on cloud-top height for mesoscale numerical model simulations. *Geoscientific Model Development*, *6*, 429–443. https://doi.org/10.5194/gmd-6-429-2013

Zaveri, R. A., Easter, R. C., Fast, J. D., & Peters, L. K. (2008). Model for simulating aerosol interactions and chemistry (MOSAIC). *Journal of Geophysical Research: Atmospheres*, *113*, 1–29. https://doi.org/10.1029/2007JD008782

Zaveri, R. A., Easter, R. C., & Peters, L. K. (2005). A computationally efficient Multicomponent Equilibrium Solver for Aerosols (MESA). *Journal of Geophysical Research: Atmospheres*, *110*, D24203. https://doi.org/10.1029/2004JD005618